Geophysical Journal International

*Geophys. J. Int.* (2016) **205,** 728–743
Advance Access publication 2016 January 27
GJI Geodynamics and tectonics

doi: 10.1093/gji/ggw044

# The role of elasticity in simulating long-term tectonic extension

Jean-Arthur Olive,[1,*] Mark D. Behn,[2] Eric Mittelstaedt,[3] Garrett Ito[4] and Benjamin Z. Klein[5]

[1]*Massachusetts Institute of Technology, Woods Hole Oceanographic Institution Joint Program in Oceanography, Cambridge, MA* 02139*, USA. E-mail: jaolive@ldeo.columbia.edu*
[2]*Department of Geology and Geophysics, Woods Hole Oceanographic Institution, Woods Hole, MA* 02543*, USA*
[3]*Department of Geological Sciences, University of Idaho, Moscow, ID* 83844*, USA*
[4]*Department of Geology and Geophysics, University of Hawaii, Honolulu, HI* 96822*, USA*
[5]*Department of Earth, Atmospheric and Planetary Sciences, Massachusetts Institute of Technology, Cambridge, MA* 02139*, USA*

Accepted 2016 January 25. Received 2016 January 16; in original form 2015 February 18

## SUMMARY

While elasticity is a defining characteristic of the Earth's lithosphere, it is often ignored in numerical models of long-term tectonic processes in favour of a simpler viscoplastic description. Here we assess the consequences of this assumption on a well-studied geodynamic problem: the growth of normal faults at an extensional plate boundary. We conduct 2-D numerical simulations of extension in elastoplastic and viscoplastic layers using a finite difference, particle-in-cell numerical approach. Our models simulate a range of faulted layer thicknesses and extension rates, allowing us to quantify the role of elasticity on three key observables: fault-induced topography, fault rotation, and fault life span. In agreement with earlier studies, simulations carried out in elastoplastic layers produce rate-independent lithospheric flexure accompanied by rapid fault rotation and an inverse relationship between fault life span and faulted layer thickness. By contrast, models carried out with a viscoplastic lithosphere produce results that may qualitatively resemble the elastoplastic case, but depend strongly on the product of extension rate and layer viscosity $U \times \eta_L$. When this product is high, fault growth initially generates little deformation of the footwall and hanging wall blocks, resulting in unrealistic, rigid block-offset in topography across the fault. This configuration progressively transitions into a regime where topographic decay associated with flexure is fully accommodated within the numerical domain. In addition, high $U \times \eta_L$ favours the sequential growth of multiple short-offset faults as opposed to a large-offset detachment. We interpret these results by comparing them to an analytical model for the fault-induced flexure of a thin viscous plate. The key to understanding the viscoplastic model results lies in the rate-dependence of the flexural wavelength of a viscous plate, and the strain rate dependence of the force increase associated with footwall and hanging wall bending. This behaviour produces unrealistic deformation patterns that can hinder the geological relevance of long-term rifting models that assume a viscoplastic rheology.

**Key words:** Mid-ocean ridge processes; Continental tectonics: extensional; Lithospheric flexure; Mechanics, theory, and modelling.

## 1 INTRODUCTION

The Earth's lithosphere is commonly defined as the outermost mechanical layer that can withstand large deviatoric stresses ($\sim 10^2$–$10^3$ MPa) before it yields, either through brittle failure or more or less localized viscous creep (e.g. Murrell 1976; Goetze & Evans 1979; Watts & Burov 2003). Consequently, the brittle upper portion of the lithosphere where tectonic faulting occurs does not undergo diffuse viscous deformation at time scales characteristic of mantle convection or plate boundary processes. In fact, the deformation of the lithosphere is often described as being elastic. Short-term tectonic processes occurring over seconds to months (e.g. seismic wave propagation or coseismic stress changes) are accounted for by linear elastic models (e.g. King *et al*. 1994; Segall 2010).

*Now at: Lamont-Doherty Earth Observatory, Columbia University, Palisades, NY 10964, USA.

Linear elastic models are also used to describe some long-term processes ($10^5$–$10^7$ yr) including lithospheric flexure in response to seamount loading, subduction, and active faulting, which are all well modelled by the deflection of a thin elastic plate (e.g. Watts 2001). Interestingly, elastic models often do a good job at predicting flexural patterns even in regions where brittle failure is known to be pervasive. For example, the long-wavelength topography of outer rises near subduction zones is well predicted by elastic plate models (e.g. Turcotte & Schubert 2002) even though widespread normal faulting, indicative of brittle failure of the lithosphere, is documented in these settings (e.g. Ranero *et al*. 2003; Zhang *et al*. 2014; Zhou *et al*. 2015). Elastic rheology therefore underlies the behaviour of the lithosphere over a range of spatial and temporal scales, and stress conditions.

Despite its importance in plate tectonic processes, elastic rheology is absent from many numerical geodynamic models, which treat the lithosphere as a high-viscosity viscoplastic solid. This description can be simpler to implement in a Stokes flow solver because it does not require tracking the build-up of stresses over time. Billen (2008) justified this 'viscous approximation' in models of subducting slabs stating 'over long times (greater than approximately 1 Myr) the elastic response of the lithosphere and mantle can be ignored and only the viscous or viscoplastic behaviour [can be] considered'. However, it is not clear that this assumption is valid in the cooler, more rigid parts of the lithosphere, where long relaxation time scales allow elastic flexure to remain pronounced up to ∼100 Myr following the onset of lithospheric loading (Watts & Zhong 2000).

Further, Kaus & Becker (2007) showed that while elasticity has little influence on the development of Rayleigh–Taylor instabilities with viscosities and density contrasts representative of mantle convection and sublithospheric flow conditions, incorporating elasticity significantly changes the patterns of stress accumulation throughout the model domain. One might therefore expect a key role of elasticity in problems involving plate flexure and buckling instabilities (Schmalholz & Podlachikov 1999; Kaus & Podlachikov 2006). This has been confirmed in recent numerical modelling studies that document the role of elasticity on the retreat and flexural behaviour of subducting slabs (Farrington *et al*. 2014; Fourel *et al*. 2014). In addition, models of long-term lithospheric deformation that involve spontaneous strain localization (e.g. faulting, subduction initiation, mountain building and rifting) may also be sensitive to the incorporation of elasticity due to its influence on stress accumulation in the lithosphere. This study aims at identifying the consequences of the viscoplastic approximation on a well-studied geodynamic problem that involves both localized brittle failure and lithospheric flexure: the growth of rift-bounding normal faults at extensional plate boundaries.

Many numerical models of rifting do not include elasticity (e.g. Behn *et al*. 2002; Allken *et al*. 2011, 2012, 2013; Gerya 2010b, 2013; Püthe & Gerya 2013) and treat the oceanic lithosphere or brittle upper crust as a high viscosity viscoplastic layer. However, in the context of long-term tectonic rifting models, the importance of elasticity may be twofold. First, the relevant deformation time scale in such models is not the duration of the simulation, but the life span of individual normal faults, which can be as short as $\sim 10^4$ yr depending on geological parameters and extension rate (e.g. Buck *et al*. 2005; Behn & Ito 2008). Second, numerous studies have shown that normal fault evolution is controlled by the build-up of elastoplastic stresses in the faulted layer (Forsyth 1992; Buck 1993; Lavier *et al*. 2000; Lavier & Buck 2002). This build-up is generally attributed to the flexural readjustment of the footwall and hanging wall blocks in response to fault growth (Buck 1988; King *et al*. 1988; Weissel & Karner 1989), and has consequences for both fault rotation (Olive & Behn 2014; Olive *et al*. 2014) and fault life span, that is, whether a single fault can grow indefinitely or whether it will be abandoned in favour of a new, spontaneously forming fault (Forsyth 1992; Buck 1993; Lavier *et al*. 2000; Behn & Ito 2008). It is therefore unclear to what extent a viscoplastic description of the lithosphere will produce behaviours that are relevant for natural extensional systems.

To address these issues, we compare numerical simulations of extension carried out within the same numerical code, assuming either a viscoplastic or an elastoplastic brittle layer. We identify and interpret the discrepancies between the two sets of simulations with the help of semi-analytical models of flexure in elastic and viscous thin plates.

## 2 METHODS

To assess the effect of elasticity on the development of normal faults, we performed simulations of extension on a single fault in uniform brittle layers of varying thicknesses over a range of extension rates, both with and without elasticity. We systematically characterized fault-induced topography, fault dip, and fault life span from each of these simulations.

### 2.1 Numerical methodology

Our simulations were carried out using SiStER (Simple Stokes solver with Exotic Rheologies), a 2-D finite-difference/particle-in-cell code (Harlow & Welch 1965; Gerya & Yuen 2003, 2007) written in MATLAB®, and based on the methodology of Gerya (2010a). This code relies heavily on MATLAB (built-in) functions and capabilities for vector operations, and achieves computation speeds on par with standard serial compiled language codes. We solve for conservation of mass, momentum and energy in a 2-D continuum assuming material incompressibility:

$$\frac{\partial v_i}{\partial x_i} = 0 \tag{1}$$

$$\frac{\partial \sigma'_{ij}}{\partial x_j} - \frac{\partial P}{\partial x_i} + \rho g_i = 0 \tag{2}$$

$$\rho c_P \frac{\mathrm{D}T}{\mathrm{D}t} = \frac{\partial}{\partial x_i}\left(k \frac{\partial T}{\partial x_i}\right), \tag{3}$$

where $v_i$, $\sigma'_{ij}$ and $T$ denote velocities, deviatoric stresses, and temperature, respectively (see Table 1 for a summary of notations). Repeated indices imply summation and the first term in eq. (3) is the material time-derivative of $T$. These equations are discretized on an Eulerian (non-deforming) grid using a conservative finite difference scheme on a fully staggered grid (Gerya 2010a; Duretz *et al*. 2011). The matrix equation for the discretization is defined in terms of the two velocity components and pressure, and then solved using the direct 'backslash' solver in MATLAB. Non-linear terms in eq. (2) are handled by performing Picard-type iterations at each time step. During each Picard iteration, non-Newtonian viscosity terms in the stress-strain rate relation (see Sections 2.2 and 2.3) are updated using the strain rate from the latest velocity solution, and then discretized to solve eq. (2) and obtain the next velocity solution. This process is repeated until the strain rate field changes by no more than 1 per cent in less than 10 per cent of the area of the model domain.

**Table 1.** Summary of parameter notations.

| Symbol | Definition | Value |
|---|---|---|
| $v_i$ | Velocity field with components ($v_x$, $v_y$) | |
| $P$ | Pressure field | |
| $\sigma'_{ij}$, $\Delta\sigma'_{ij}$, | Deviatoric stress tensor, stress increment | |
| $\sigma'_{\mathrm{II}}$ | Second invariant of the deviatoric stress tensor | |
| $\sigma_y$, $\Delta\sigma_y$ | Yield stress, strength contrast between fault zone and intact lithosphere | |
| $\dot{\epsilon}_{II}$ | Second invariant of the strain rate tensor | |
| $g$ | Gravitational acceleration | 9.81 m s$^{-2}$ |
| $\rho$ | Density field | |
| $\rho_{\mathrm{R}}$ | Density of the faulted layer and underlying asthenosphere | 3300 kg m$^{-3}$ |
| $\rho_{\mathrm{O}}$ | Density of the ocean layer | 1000 kg m$^{-3}$ |
| $\Delta\rho$ | Density contrast between the faulted layer and the overlying fluid layer | 2300 kg m$^{-3}$ |
| $T$ | Temperature field | |
| $\Delta t$ | Time step | |
| $Z$ | Viscoelastic ratio | |
| $G$ | Shear modulus | 10 GPa |
| $\nu$ | Poisson's ratio | 0.5 |
| $E$ | Young's modulus | 30 GPa |
| $\eta$ | Viscosity field | |
| $\eta_{\mathrm{REF}}$ | Reference viscosity (temperature-dependent) | |
| $\eta_{\mathrm{PLAS}}$ | Plastic viscosity | |
| $\eta_{\mathrm{L}}$ | Viscosity of the faulted layer | $10^{24\text{-}25}$ Pa s |
| $\eta_{\mathrm{WEAK}}$ | Viscosity of the sticky layer and asthenosphere | $10^{-6}$ $\eta_{\mathrm{L}}$ |
| $\dot{\Omega}$ | Rotation rate | |
| $U$ | Full extension rate | |
| $H$ | Faulted layer thickness | |
| $h$ | Fault heave | |
| $h_{\mathrm{CRIT}}$, $\varepsilon_{\mathrm{CRIT}}$ | Critical offset and strain on the fault necessary for full cohesion weakening | 100 m |
| $\varepsilon_{\mathrm{P}}$ | Accumulated plastic strain | |
| $\tau_{\mathrm{H}}$ | Healing time scale | 3100 m U$^{-1}$ |
| $C_{\mathrm{MAX}}$, $C_{\mathrm{MIN}}$ | Maximum and minimum value of cohesion | 135 and 0.01 MPa |
| $\mu$ | Friction coefficient | 0.53 |
| $\theta$ | Dip of the fault | |
| $\alpha$, $\alpha_{\mathrm{E}}$, $\alpha_{\mathrm{V}}$ | Flexural parameter, flexural wavelength of an elastic / viscous layer | |
| $D$ | Flexural rigidity of an elastic layer | |
| $L$ | Width of the numerical model | |

Advection is handled by moving tracer particles, which passively carry material properties in the velocity field with a fourth-order Runge–Kutta method (in space) over an advection time step $\Delta t$. The time step is set so that markers move only by half of the smallest cell size during each time iteration (i.e. 50 per cent of the Courant condition). Properties are passed between nodes and particles through bilinear interpolation (Gerya 2010a). In particular, the advection term in eq. (3) is handled by the motion of markers, while the remaining diffusion equation is solved with an explicit finite difference scheme.

### 2.2 Implementation of viscoelasticity

In order to close the system of conservation eqs (1)–(3), we assume a Maxwell linear stress-strain rate relationship of the form

$$\dot{\epsilon}_{ij} = \frac{1}{2\eta}\sigma'_{ij} + \frac{1}{2G}\frac{D\sigma'_{ij}}{Dt}. \tag{4}$$

This type of material behaves elastically when deformed over a time scale shorter than its Maxwell characteristic time $\tau_{\mathrm{M}}$

$$\tau_{\mathrm{M}} = \frac{\eta}{G}. \tag{5}$$

Following Moresi *et al.* (2003), we discretize the Eulerian part of the material derivative $\frac{D\sigma'_{ij}}{Dt}$ using backward finite difference over the advection time step $\Delta t$, yielding

$$\dot{\epsilon}_{ij} = \frac{1}{2\eta}\sigma'_{ij} + \frac{1}{2G}\frac{\sigma'^{(t)}_{ij} - \sigma'^{(t-\Delta t)}_{ij}}{\Delta t}. \tag{6}$$

From eq. (6), we can rewrite the stress–strain relationship at time $t$:

$$\sigma'_{ij} = 2\eta Z\dot{\epsilon}_{ij} + (1 - Z)\,\sigma'^{(t-\Delta t)}_{ij} \tag{7}$$

in which we introduce a viscoelastic ratio $Z$

$$Z = \frac{G\Delta t}{G\Delta t + \eta}. \tag{8}$$

Upon inserting eq. (7) into eq. (2), conservation of momentum can be rewritten as

$$\frac{\partial}{\partial x_j}\left(2\eta Z\dot{\epsilon}_{ij}\right) - \frac{\partial P}{\partial x_i} + \rho g_i = -\frac{\partial}{\partial x_j}\left[(1 - Z)\,\sigma'^{(t-\Delta t)}_{ij}\right]. \tag{9}$$

In this formulation, the viscoelastic ratio acts to modify the effective viscosity ($\eta Z$) in the stress divergence term, and the elasticity terms appear as a stress history term on the right-hand side. If one sets a viscosity $\eta$ that is high enough such that $\eta \gg G\Delta t$ (i.e. $\Delta t \ll \tau_{\mathrm{M}}$), the material effectively behaves elastically ($Z \approx 0$). By contrast, setting an unrealistically high shear modulus such that $G\Delta t \gg \eta$ turns off all elastic effects ($Z \approx 1$). This framework allows distinct portions of the numerical domain to behave in a purely viscous, purely elastic, or in a viscoelastic fashion. It also enables direct comparisons of simulations with and without elasticity.

Deviatoric stress is carried on particles (Gerya 2010a; Keller *et al*. 2013). Every time a velocity solution is obtained, the current strain rate field is used to update the deviatoric stress ${\sigma'_{ij}}^{(t-\Delta t)}$ by adding the stress increment $\Delta\sigma'_{ij}$, (after eq. (7)):

$$\Delta\sigma'_{ij} = Z\left[2\eta\dot{\epsilon}_{ij} - {\sigma'_{ij}}^{(t-\Delta t)}\right]. \tag{10}$$

The stresses are then advected with the particles and rotated using the local rotation rate $\dot{\Omega}$ :

$$\dot{\Omega} = \frac{1}{2}\left(\frac{\partial v_y}{\partial x} - \frac{\partial v_x}{\partial y}\right), \tag{11}$$

and the following rotation formulae over a time step $\Delta t$ (Gerya 2010a):

$$\begin{cases} {\sigma'_{xx}}^{\text{ROTATED}} = \sigma'_{xx}\left[\cos^2\left(\dot{\Omega}\Delta t\right) - \sin^2\left(\dot{\Omega}\Delta t\right)\right] \\ \qquad\qquad -\sigma'_{xy}\sin\left(2\dot{\Omega}\Delta t\right) \\ {\sigma'_{xy}}^{\text{ROTATED}} = \sigma'_{xx}\sin^2\left(\dot{\Omega}\Delta t\right) + \sigma'_{xy}\cos\left(2\dot{\Omega}\Delta t\right) \end{cases}. \tag{12}$$

### 2.3 Implementation of plasticity for simulating faulting

In addition to the modifications due to the elastic terms, the effective viscosity $\eta$ used in eq. (9) can also be modified to account for non-Newtonian material creep and plasticity. We account for material plasticity by lowering the effective viscosity wherever the second invariant of the deviatoric stresses ($\sigma'_{\text{II}}$) exceeds the yield stress ($\sigma_y$). This is done by harmonically averaging the prescribed (Newtonian) reference viscosity $\eta_{\text{REF}}$ with a 'plastic viscosity' $\eta_{\text{PLAS}}$ (e.g. Behn *et al*. 2007):

$$\eta = \left(\frac{1}{\eta_{\text{REF}}} + \frac{1}{\eta_{\text{PLAS}}}\right)^{-1}, \tag{13}$$

where $\eta_{\text{PLAS}}$ depends on the yield stress and the second invariant of the strain rate:

$$\eta_{\text{PLAS}} = \frac{\sigma_y}{2\dot{\epsilon}_{\text{II}}}. \tag{14}$$

The yield stress is calculated using a Drucker–Prager failure criterion:

$$\sigma_y = AP_{\text{L}} + B, \tag{15}$$

where $P_{\text{L}}$ is the lithostatic part of the pressure field, estimated by integrating the weight of the overlying material. The constants $A$ (0.47) and $B$ (120 MPa) are chosen to approximate a Mohr–Coulomb criterion (with lithostatic mean stress) with a friction coefficient $\mu = 0.53$ and initial cohesion $C_{\text{MAX}} = 135$ MPa.

Plastic strain accumulates wherever the failure criterion (eq. 15) is met, following:

$$\frac{\partial\epsilon_P}{\partial t} = \begin{Bmatrix} \dot{\epsilon}_{\text{II}} & \text{if } \sigma'_{\text{II}} \geq \sigma_y \\ 0 & \text{if } \sigma'_{\text{II}} < \sigma_y \end{Bmatrix} - \frac{\epsilon_P}{\tau_H} \tag{16}$$

where $\sigma'_{\text{II}}$ designates the second invariant of the deviatoric stress tensor. $\dot{\epsilon}_{\text{II}}$ is the second invariant of the strain rate tensor, which in yielded zones is approximately equal to the plastic strain rate. The second term on the right-hand side of eq. (16) simulates a healing mechanism (Poliakov & Buck 1998), which progressively reduces the accumulated plastic strain over a relatively long-time scale ($\tau_H$). This formulation promotes the build-up of plastic strain in regions of sustained localized shear (high strain rate) and healing in regions of diffuse plastic yielding. In this study, the healing time is scaled with the extension rate such that $U \times \tau_H = 3100$ m. This is done to prevent excessive fault healing in simulations with very slow extension rates, which must be carried out over a much longer time to reach the same amount of total extension. Rapid fault healing helps to sustain localized deformation within narrow fault-like zones. It also enables deformation to relocalize quickly onto a new fault when an older fault is abandoned.

To further promote strain localization, cohesion is decreased linearly with accumulated plastic strain ($\varepsilon_P$) until a critical plastic strain ($\varepsilon_{\text{CRIT}}$) corresponding to an amount of fault slip ($h_{\text{CRIT}}$) is reached (e.g. Lavier *et al*. 2000), at which point cohesion (initially $C_{\text{MAX}}$) reaches a minimum value ($C_{\text{MIN}}$). Since the width of localized shear zones in continuum mechanics models is typically ~3 elements, we adapt the value of $\varepsilon_{\text{CRIT}}$ to the grid size so that full fault weakening corresponds to a critical fault offset $h_{\text{CRIT}}$, which does not depend on grid resolution (Lavier *et al*. 2000). Specifically, $\varepsilon_{\text{CRIT}}$ is set to $h_{\text{CRIT}}$ divided by 3 times the grid size. The simulations presented here use $h_{\text{CRIT}} = 100$ m, which enables fast weakening and rapid strain localization.

Finally, in eq. (13), $\eta_{\text{REF}}$ can be set by a material flow law relating it to temperature, pressure, strain rate and additional parameters such as grain size. In this study, we restrict ourselves to a simple temperature-dependent Newtonian flow law:

$$\log_{10}(\eta_{\text{REF}}) = \log_{10}(\eta_{\text{WEAK}}) + \frac{1}{2}\log_{10}\left(\frac{\eta_{\text{L}}}{\eta_{\text{WEAK}}}\right) \times\left[1 - \frac{2}{\pi}\tan^{-1}\left(\frac{T - T_{\text{C}}}{w_T}\right)\right]. \tag{17}$$

This functional form ensures that any material that is colder than $T_{\text{C}} = 600\,^{\circ}$C and is not undergoing plastic yielding will be assigned a high viscosity $\eta_{\text{L}}$, whereas material hotter than $T_{\text{C}}$ is assigned a low viscosity $\eta_{\text{WEAK}}$. A small value of $w_T$ (1 °C) ensures a sharp drop in viscosity at the 600 °C isotherm.

### 2.4 Model setup

The model consists of a brittle (faulted) lithosphere layer of thickness $H = 10$–$30$ km sandwiched between two weak layers of equal thicknesses (comparable to $H$) representing an overlying ocean (also referred to as a 'sticky' layer, Crameri *et al*. 2012) and underlying asthenosphere (Fig. 1). Ocean and rock densities are $\rho_{\text{O}} = 1000$ kg m$^{-3}$ and $\rho_{\text{R}} = 3300$ kg m$^{-3}$, respectively. Horizontal extension is imposed symmetrically on the two vertical sides at full rates $U = 0.02$–$20$ cm yr$^{-1}$. All boundaries are free slip. The top and bottom have prescribed influx conditions so as to

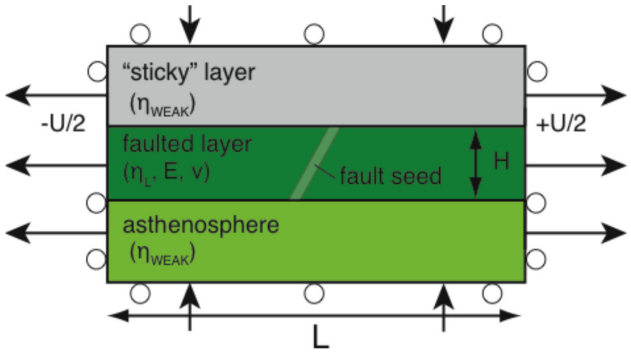


**Figure 1.** Schematic setup of our numerical models for fault evolution in an elastoplastic or a viscoplastic layer sandwiched between two viscous layers. A single 50°-dipping fault is seeded at the first time iteration as a thin band of low-cohesion material, and then allowed to evolve freely as strain localizes along this narrow shear band.

balance the flux out the sides. New markers are added to the domain wherever the marker density drops below 80 per cent of its initial value. These 'reseeded' markers are assigned properties that are interpolated from nodal values, or averaged from the properties of neighbouring markers (for quantities that are never passed to and modified on nodes, such as plastic strain or deviatoric stresses).

The flow law in eq. (17) defines the geometry of the layers based on the temperature field, with the 600 °C isotherm acting as the approximate brittle–ductile transition that marks the base of the faulted layer. The initial temperature field increases linearly with depth in the brittle layer and asthenosphere, with gradients set to produce the desired brittle layer thickness. Temperature throughout the sticky (top) layer is maintained at 0 °C. Conservation of energy (eq. 3) is solved assuming adiabatic sides and Dirichlet boundary conditions along the top ($T = 0$ °C) and bottom ($T = 1000$ °C). We use a thermal diffusivity ($k/\rho c_P$) that is uniform throughout the domain and set to $10^{-5}$ m$^2$ s$^{-1}$. This value is an order of magnitude greater than that expected in geological systems, and high enough to maintain a linear thermal gradient in the lithosphere and asthenosphere as extension proceeds. This setup allows the faulted layer to retain its initial thickness $H$ while it is extended by amounts much greater than $H$, over a wide range of extension rates. This simplifying assumption enables direct comparisons with the classic study of finite extension in a constant-thickness elastoplastic layer of Lavier *et al.* (2000).

Following eq. (17), the brittle layer ($T < 600$ °C) has a uniform viscosity $\eta_L$ (set to $10^{24}$ or $10^{25}$ Pa s depending on the simulation), while the asthenosphere ($T \geq 600$ °C) has a viscosity $\eta_{WEAK} = 10^{-6} \times \eta_L$. We impose a uniform low viscosity $\eta_{WEAK}$ in the sticky layer. The shear modulus of the two weak layers (sticky layer and asthenosphere) is set to the unrealistically high value of $10^{19}$ GPa, resulting in a very short Maxwell time (eq. 5), which ensures that they behave viscously. Simulations with an elastoplastic faulted layer use a Young's modulus and Poisson's ratio of $E = 30$ GPa and $\nu = 0.5$ (incompressible) in the faulted layer, yielding $G = 10$ GPa, and a Maxwell time of 3–30 Myr for the lithosphere. By contrast, simulations with a viscoplastic (no elasticity) faulted layer were carried out with a shear modulus of $10^{19}$ GPa throughout the domain.

To ensure that a single normal fault develops in the center of the model domain, we initialize the model with a rectangular (one element-wide) 'fault seed' dipping at an angle $\theta_0 = 50°$ throughout the faulted layer. This orientation is compatible with the model setup and assumed plastic properties (Kaus 2010). Within the fault seed, plastic strain is set to its critical value $\varepsilon_{CRIT}$, and cohesion is fully weakened accordingly. The box width ($L$) is set to three times the elastic flexural wavelength of the faulted layer $\alpha_E$, which is given by

$$\alpha_E = \left(\frac{4D}{\Delta\rho g}\right)^{\frac{1}{4}}, \tag{18}$$

where $\Delta\rho = 2300$ kg m$^{-3}$ is the density contrast between the faulted layer and the overlying ocean, and $D$ is the flexural rigidity of the elastic layer:

$$D = \frac{E H^3}{12(1-\nu^2)}. \tag{19}$$

For faulted layers with viscoplastic rheology, the reference box width is the same as their elastoplastic counterparts to allow for direct comparison; subsequent calculations include wider boxes as motivated by the initial findings. The grid resolution close to the fault is refined to ~1 km or less (<500 m in cases with $H < 15$ km).

**Table 2.** Summary of numerical simulations. 'Faulting regime' denotes either 'prolonged slip' ($\infty$) on the initial fault, or 'multiple faults' (MF) forming in sequence. For MF simulations, the maximum horizontal offset accommodated on the initial fault is indicated in parentheses.

| Name | Elasticity? | $\eta_L$ (Pa s) | $H$ (km) | $U$ (cm yr$^{-1}$) | $L$ (km) | Faulting regime |
|---|---|---|---|---|---|---|
| E10slow | On | $10^{25}$ | 10 | 0.2 | 84 | $\infty$ |
| E10ref | On | $10^{24}$ | 10 | 2 | 84 | $\infty$ |
| E10fast | On | $10^{24}$ | 10 | 20 | 84 | $\infty$ |
| E20slow | On | $10^{25}$ | 20 | 0.2 | 140 | MF (14 km) |
| E20ref | On | $10^{24}$ | 20 | 2 | 140 | MF (13 km) |
| E20fast | On | $10^{24}$ | 20 | 20 | 140 | MF (13 km) |
| E30slow | On | $10^{25}$ | 30 | 0.2 | 190 | MF (6 km) |
| E30ref | On | $10^{24}$ | 30 | 2 | 190 | MF (4 km) |
| E30fast | On | $10^{24}$ | 30 | 20 | 190 | MF (5 km) |
| V10slow | Off | $10^{24}$ | 10 | 0.2 | 84 | $\infty$ |
| V10slow_25 | Off | $10^{25}$ | 10 | 0.2 | 84 | MF (14 km) |
| V10ref | Off | $10^{24}$ | 10 | 2 | 84 | MF (15 km) |
| V10fast | Off | $10^{24}$ | 10 | 20 | 84 | MF (10 km) |
| V20slow | Off | $10^{24}$ | 20 | 0.2 | 140 | $\infty$ |
| V20ref | Off | $10^{24}$ | 20 | 2 | 140 | MF (46 km) |
| V20fast | Off | $10^{24}$ | 20 | 20 | 140 | MF (9 km) |
| V30slow | Off | $10^{24}$ | 30 | 0.2 | 190 | Incomplete localization |
| V30ref | Off | $10^{24}$ | 30 | 2 | 190 | MF (15 km) |
| V30fast | Off | $10^{24}$ | 30 | 20 | 190 | MF (10 km) |
| E10fast_LB | On | $10^{24}$ | 10 | 20 | 252 | $\infty$ |
| V10slow_LB | Off | $10^{24}$ | 10 | 2 | 252 | $\infty$ |
| V10fast_LB | Off | $10^{24}$ | 10 | 20 | 252 | MF (9 km) |

## 3 NUMERICAL RESULTS

Numerical simulations reaching up to 22 km of total extension were performed for 19 cases varying different model parameters including $H$, $U$ and $\eta_L$. Model parameters for all simulations are summarized in Table 2. Note that the 'slow' ($U \leq 0.2$ cm yr$^{-1}$) elastoplastic runs require a higher $\eta_L$ ($10^{25}$ Pa s) to ensure that the duration of the entire simulation remains shorter than the Maxwell time of the faulted layer (and the layer therefore remains elastic throughout the run).

### 3.1 Generic model behaviour

In 18 out of 19 simulations (Table 2), the applied extensional strain localized spontaneously onto the 50°-dipping fault seed at the centre of the brittle layer, within the first few time iterations. This results in a ~3 element wide fault zone of reduced strength where plastic strain increases rapidly (Fig. 2). As the fault accumulates horizontal offset ($h$), the adjacent blocks undergo flexure (especially the footwall), and topography grows (Figs 2a and b). Tensile and compressional bending stresses accumulate in the bottom- and top-half of the footwall block, respectively. These stresses reach the yield strength (hundreds of MPa) in a large part of the faulted layer (Figs 2g and h). Consequently, the layer viscosity is reduced below its 'unyielded' value of $\eta_L$, which is indicative of widespread diffuse yielding (Figs 2e and f). Yielding is initially too distributed (and the strain rate is too low) for plastic strain to accumulate significantly outside of the initial fault zone (Figs 2c and d). However, in some cases where high footwall stresses are sustained (e.g. Figs 2f and h) failure can become localized and lead to the formation of a second fault. The second fault will then replace the initial fault and take up the full plate separation (e.g. Figs 3a–c, h, i, k and l).

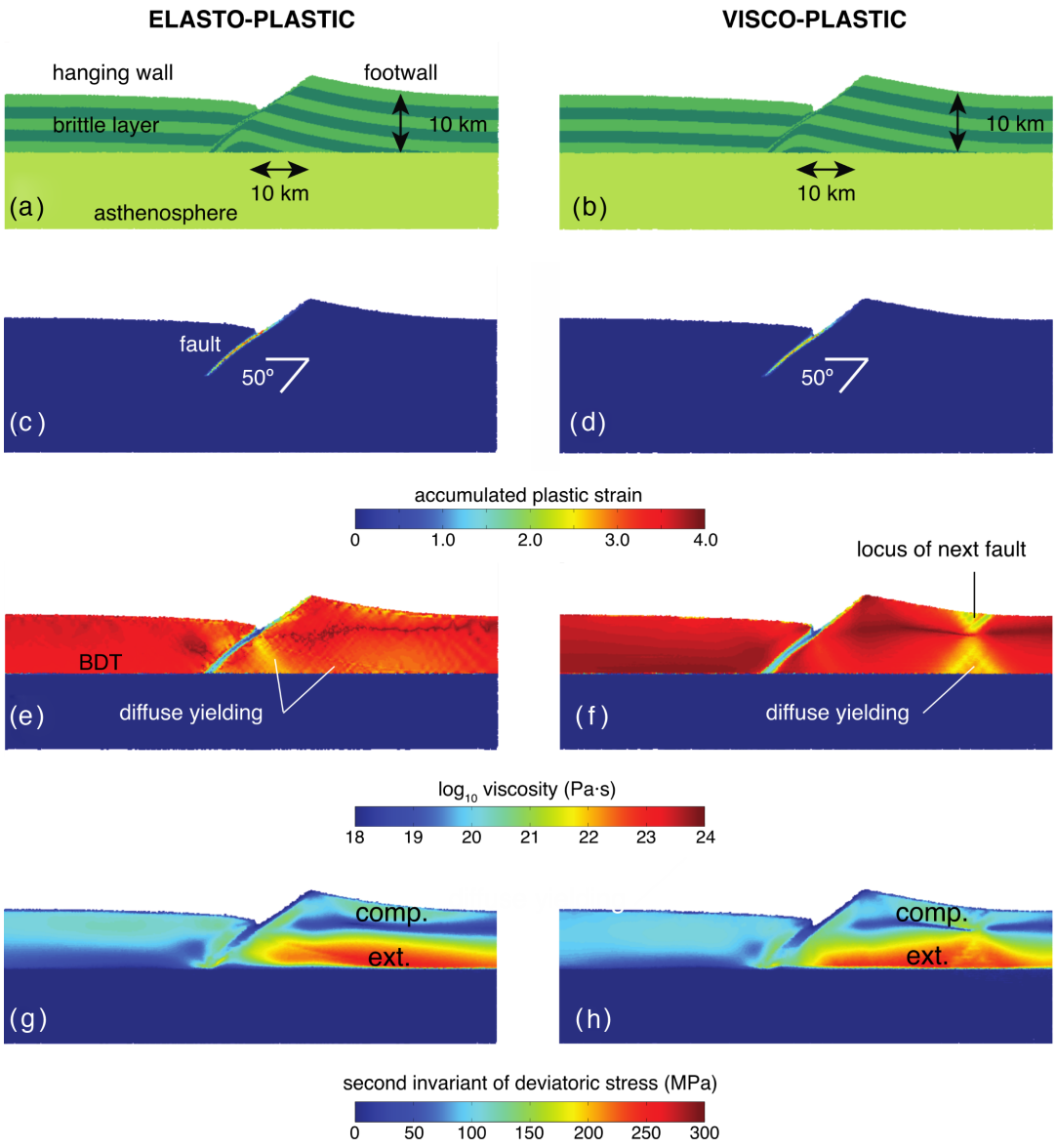


**Figure 2.** Comparison of an elastoplastic (left-hand column) and a viscoplastic (right-hand column) simulation with $H = 10$ km, $U = 2$ cm yr$^{-1}$, and $\eta_L = 10^{24}$ Pa s, after 10 km of extension. (a) and (b): Internal deformation in the faulted layer, visualized through the folding of initially horizontal, 2-km-thick strata. (c) and (d): Accumulated plastic strain revealing fault rotation from an initial angle of 50°. (e) and (f): Layer viscosity revealing localized yielding in the fault zone and diffuse yielding outside the fault zone, wherever viscosity is lower than $10^{24}$ Pa s. BDT, brittle–ductile transition (600 °C isotherm). (g) and (h): Second invariant of the deviatoric stress tensor showing the distribution of flexural stresses.

We call this behaviour the 'multiple faults' regime (Lavier *et al.* 2000), as opposed to cases where the initial fault slips indefinitely without being abandoned, which we refer to as the 'prolonged slip' regime (e.g. Figs 3d–f, j). While the distribution of stresses around the initial fault look qualitatively similar between elastoplastic and viscoplastic simulations (Figs 2g and h), the geometry of the yielded zone may show striking differences. For example, slip along a fault in a 10-km thick elastoplastic brittle layer at 2 cm yr$^{-1}$ results in diffuse weakening of the footwall and hanging wall in close proximity to the fault (Fig. 2e), which does not localize to form a new fault. By contrast, the same simulation in a viscoplastic layer does not produce weakening adjacent to the fault, but rather about 30 km away in the footwall (Fig. 2f). This initially diffuse yielded zone eventually localizes into a new fault that takes up the entire plate separation. In other situations the second fault can form on the hanging wall side by a similar mechanism (Fig. 3). This suggests that the formation of a second fault occurs under a very different set of parameters in viscoplastic versus elastoplastic simulations.

In the following sections, we report on specific differences between viscoplastic and elastoplastic models regarding the growth of topography (Section 3.2), the rotation of the initial fault (Section 3.3), and the modes of extensional faulting (Section 3.4). To study topographic growth and fault rotation, we focus on the growth of the initially seeded fault focusing primarily on simulations that allow prolonged slip on the initial fault (i.e. utilizing thinner faulted layers, as detailed in Section 3.4).

### 3.2 Fault-induced topography

In all simulations with an elastoplastic rheology, the relief associated with fault growth systematically features a short wavelength

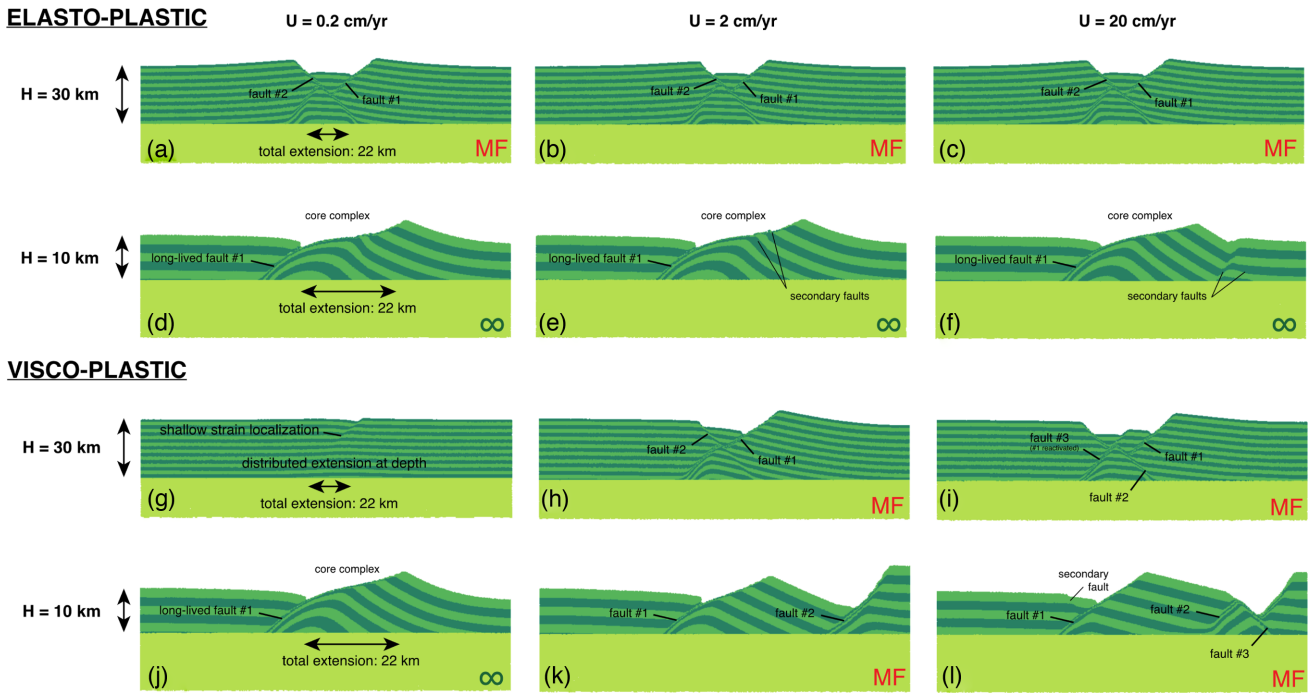


**Figure 3.** Snapshots of internal deformation after 22 km of extension in several elastoplastic (a)–(f) and viscoplastic (g)–(l) simulations with varying faulted layer thickness and extension rate. The darker-green strata were initially 2 km thick, and lying horizontally at the beginning of the simulation. The lightest-green layer is the asthenosphere, separated from the faulted layer by the 600 °C isotherm. MF, multiple faults regime; ∞, prolonged-slip regime (see Fig. 6). All simulations have $\eta_L = 10^{24}$ Pa s. Panels (e) and (k) correspond to the simulations shown in Fig. 2, at a later time.

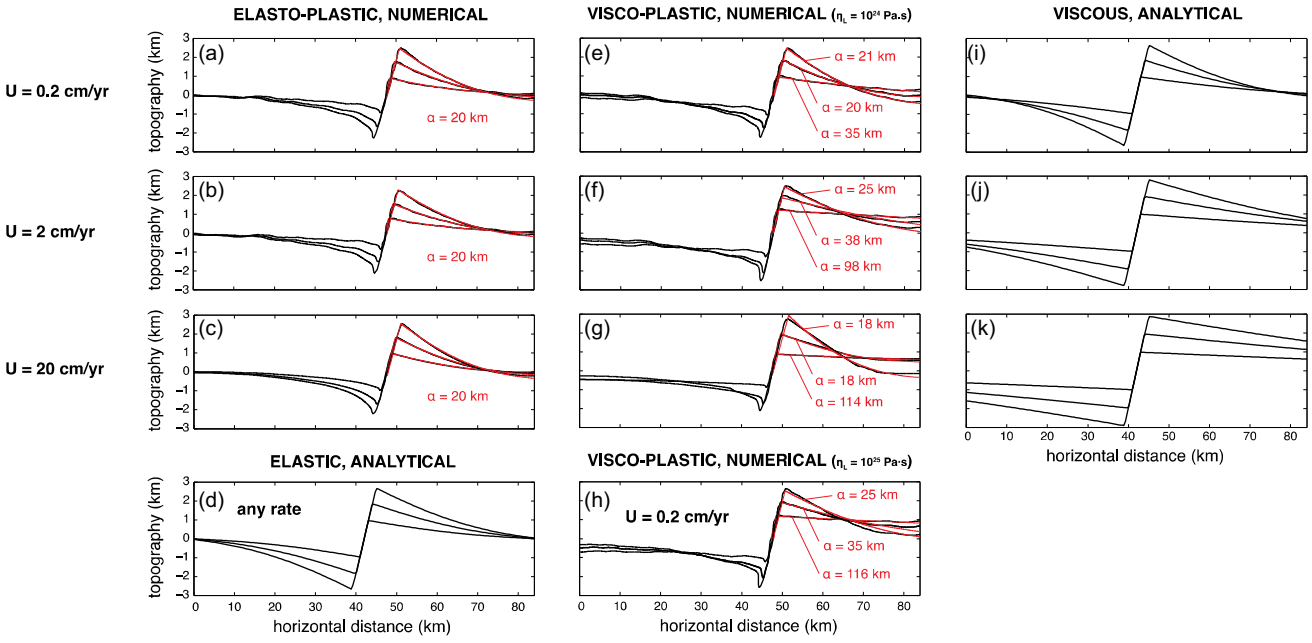


**Figure 4.** Topography (black lines) induced by 2, 4 and 6 km of horizontal offset on a normal fault growing at different extension rates in a $H = 10$-km-thick layer of varying rheology: (a) and (c) elastoplastic (numerical model), (d) purely elastic (analytical, with a displacement discontinuity at the fault), (e)–(h) viscoplastic (numerical) and (i)–(k) purely viscous (analytical). The thin red lines show the analytical solution (eq. 20) with the value of flexural wavelength $\alpha$ (in red) that best fits the numerical solution.

(~$h$) component corresponding to the fault scarp, and a longer wavelength decay of topography away from the fault. The latter component is well described as the flexure of a thin elastic plate under gravity (e.g. Weissel & Karner 1989; Olive & Behn 2014), with deflection that is anti-symmetric about the fault and decays within a few tens of km away from the fault (Figs 4a–d). The characteristic length scale of topographic decay increases systematically with faulted layer thickness (Fig. 3). In addition, the topography in all elastoplastic runs appears to be solely a function of the amount of horizontal extension accommodated on the fault, and is largely insensitive to the rate of extension.

The viscoplastic simulations also predict the short wavelength topography associated with the fault offset (fault scarp). Unlike the elastoplastic cases, however, the viscoplastic models predict a long-wavelength topography that is strongly sensitive to extension rate and the total amount of extension. At low extension rates and large fault heaves ($U = 0.2$ cm yr$^{-1}$ and $h = 4$ and 6 km, Fig. 4e), the model domain is wide enough to encompass the long-wavelength topography and the viscoplastic model predicts topographic decay with distance from the fault that is qualitatively similar to the flexural topography of the elastoplastic cases. At higher extension rates and small fault heaves (e.g. $U = 20$ cm yr$^{-1}$ and $h = 2$ km, Fig. 4g), however, the model domain is too narrow to capture the longer-wavelength decay of fault topography and the surfaces on the two sides of the fault appear to be offset like rigid blocks. As the fault accumulates more offset, the topographic decay systematically becomes more pronounced within the model domain. This evolution is apparent in Fig. 4(g), where the topography is flat on both sides of the fault scarp after $h = 2$ km of extension (rigid blocks), but later ($h \geq 4$ km) develops significant curvature. After ~6 km of extension the decay of topography away from the fault has become qualitatively similar to that predicted by the elastoplastic results (Fig. 4c). The transition between the initial rigid block phase and the onset of pronounced topographic decay requires less slip on the fault for lower extension rates (Figs 4e and f). Further, a simulation conducted with a slow (0.2 cm yr$^{-1}$) extension rate, but a higher faulted layer viscosity ($\eta_L = 10^{25}$ Pa s, simulation V10slow_25 in Table 2), produced rigid block behaviour at fault heaves as large as ~2 km. This suggests that greater fault slip is required to exit the rigid block phase for greater layer viscosity. The behaviour described above is observed over the whole range of simulated brittle layer thicknesses. In thicker layers, the characteristic length scale of topographic decay also decreases progressively with heave, but remains overall greater than that of thinner layers.

Finally, we tested the effect of layer viscosity on the development of topography. We find that a simulation with a faulted layer viscosity reduced by a factor of ten, but an extension rate that is increased ten times relative to another simulation, will produce the same topography as the other. This is illustrated by simulations V10slow_25 ($\eta_L = 10^{25}$ Pa s, $U = 0.2$ cm yr$^{-1}$) and V10ref ($\eta_L = 10^{24}$ Pa s, $U = 2$ cm yr$^{-1}$), in Table 2 and Figs 4(f) and (h). The evolving topography of a given run is therefore likely determined the product $U \times \eta_L$ rather than by the extension rate alone.

### 3.3 Fault dip

To assess the effect of lithospheric rheology on fault rotation kinematics, we measured the evolving dip of the seeded fault throughout all the runs by visually fitting a line through the region of greatest accumulated plastic strain (Figs 2c and d). In the elastoplastic cases, all faults are found to immediately begin rotating to a shallower dip ($\leq 40^\circ$) over a few km of accumulated heave. The rate of change in fault dip per unit of accumulated heave ($\partial\theta/\partial h$) was greatest in thinner brittle layers, which is consistent with the mechanical models presented in Olive & Behn (2014) and Olive *et al.* (2014). However, for a given layer thickness, the rotation rate ($\partial\theta/\partial h$) does not change with extension rate $U$ in a systematic manner (Fig. 5a). For example, we measured an average rate of ~2 ($\pm 0.1$)$^\circ$ km$^{-1}$ over the first 5 km of extension in all elastoplastic runs conducted with a 10-km-thick faulted layer.

In viscoplastic layers, however, the rotation rate appears to depend on both $U$ and $H$, with faster extension rates and thicker layers promoting slightly slower rotation (Figs 5b–d). For example, in cases with $H = 10$ km (Fig. 5b), the initial fault rotates at a rate of ~2.1($\pm 0.1$)$^\circ$ km$^{-1}$ over the first 5 km of extension when $U = 0.2$ cm yr$^{-1}$ (similar to the rate found in the corresponding elastoplastic simulations). By contrast, $\partial\theta/\partial h$ drops to 1.6($\pm 0.1$)$^\circ$ km$^{-1}$ in cases when $U$ is increased to 20 cm yr$^{-1}$ (Fig. 5b). Likewise, the rotation rate drops by ~30 per cent when doubling the faulted layer thickness in runs with $U = 2$ cm yr$^{-1}$ (Fig. 5d).

### 3.4 Fault life span

We next examine the longer-term evolution of the simulations, and report on the parameter combinations that favour the multiple faults regime (in which a new fault breaks and the initial fault is abandoned) versus the prolonged slip regime (in which the seeded fault never ceases to grow).

In elastoplastic layers, the prolonged slip regime occurs for layers thinner than 20 km (Fig. 6a). In this regime, sustained fault growth drives progressive flexural readjustment of the footwall, resulting in a domal structure in which the fault surface is convex up (much like a core complex in Buck 1988) near where it emerges at the surface, and transitions to concave up near the top of the fault scarp (e.g. Fig. 3d). The applied extension rate has little influence on the development and morphology of the long-lived fault, however for $U = 2$ and 20 cm yr$^{-1}$, secondary faults, which accumulate only minor total offsets, form in the footwall of the primary fault (Figs 3e and f). These secondary features are common in models of core-complex formation and are typically attributed to elastoplastic flexure in the footwall (Lavier *et al.* 2000).

For $H = 20$ km (Fig. 6a), the multiple fault regime occurs, and is characterized by the formation of a second normal fault after the initial one has accommodated ~13 km of extension (e.g. Fig. 3a). The new fault crosscuts the initial one, and systematically dips in the opposite direction. This behaviour persists for extension rates of 0.2–20 cm yr$^{-1}$ (Figs 5a–c). In thicker faulted layers ($H = 30$ km), the life span of the initial fault is even shorter (~5 km of accommodated extension), and does not change systematically with $U$. These results suggest that the transition from the prolonged slip to the multiple fault regime is mostly independent of extension rate and lies between $H = 10$–20 km (Fig. 6a). The results are also consistent with findings of previous studies that larger offsets occur on individual faults cutting through thinner elastoplastic layers (Buck 1993; Lavier *et al.* 2000; Lavier & Buck 2002; Behn & Ito 2008).

The transition between the two different fault life span regimes is very different in the viscoplastic simulations (Fig. 6b). The only two viscoplastic simulations that yielded prolonged slip on the initial fault were those carried out with the slowest extension rate of $U = 0.2$ cm yr$^{-1}$, and $H = 10$ and 20 km (Figs 3j and 6b). The structures formed in these runs look qualitatively similar to those produced in their elastoplastic counterparts. By contrast, simulations carried out with thicker faulted layers and/or faster extension rates all produced multiple faults (Figs 3h, i, k and l). Specifically, for a given $H$, we found that the faster the extension rate, the more faults formed to accommodate the same total amount of extension (Figs 3h versus i, and j versus k and l). Extension in 30-km-thick viscous layers proceeds by a succession of crosscutting faults on both plates, while extension with $H = 20$ km proceeds by parallel faults on the same plate that are a few tens of km away from each other. Further, in one of the viscoplastic simulations with $H = 30$ km (V30slow in Table 2, with $H = 30$ km and $U = 0.2$ cm yr$^{-1}$, panel A in Fig. 6), a shear band never cut through the full brittle layer,

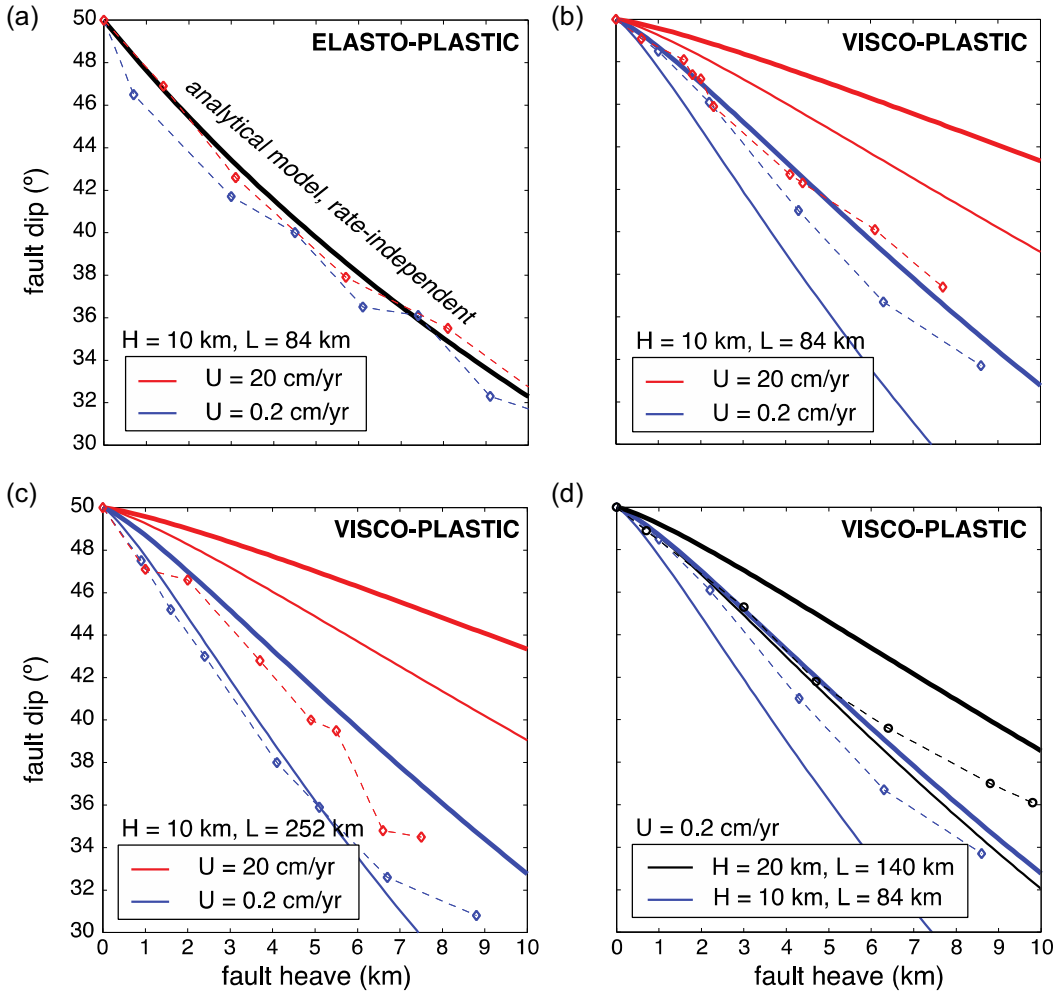


**Figure 5.** Fault rotation as a function of heave in 10-km-thick (a) elastoplastic and (b–c) viscoplastic layers, for the two extension rates labelled in (a). Model domain width in (b) is the same as in (a) for direct comparison, but is three times wider in (c) as motivated in Section 4.1. The diamonds and dashed lines indicate numerical results carried out with $\eta_L = 10^{24}$ Pa s, and the solid lines refer to analytical models (Section 4.2) for $\eta_L = 10^{24}$ (thick lines) and $10^{23}$ (thin lines) Pa s. The colour code in (b–c) corresponds to varying extension rates. (d) Effect of layer thickness on rotation kinematics in viscoplastic runs. Black symbols correspond to runs carried out with a 20-km-thick faulted layer; solid lines are as in (b) and (c).

but instead deformation localized on the fault seed within only the shallowest top 10 km (marked 'NL' for 'non-localized'). The underlying portion of the lithosphere deformed in a diffuse, pure shear manner.

Finally, we found that while the viscoplastic simulation (V10slow) with $H = 10$ km, $U = 0.2$ cm yr$^{-1}$ and $\eta_L = 10^{24}$ Pa s produced a long-lived fault, the same simulation with a 10-fold increase in brittle layer viscosity ($\eta_L = 10^{25}$ Pa s, simulation V10slow_25) evolved in the multiple faults regime (Table 2, Fig. 6b). Increasing the faulted layer viscosity by a factor of 10 therefore shifts the life span regime transition towards extension rates that are ~10 times lower. This suggests that, like the topographic evolution (Section 3.2), the faulting regime for a given faulted layer thickness is determined by the product $U \times \eta_L$. The transition is also less sensitive to the faulted layer thickness than in the elastoplastic simulations.

### 3.5 Summary of numerical results

To summarize our numerical results, we find that in elastoplastic layers fault topography, dip evolution and life span are essentially insensitive to extension rate, and closely follow the predictions of previous studies (Lavier *et al*. 2000; Behn & Ito 2008; Olive & Behn 2014). By contrast, in simulations that treat the lithosphere as a viscoplastic solid, the characteristic distance over which the long wavelength fault-induced topography decays decreases over time. The topography transitions out of a short initial phase where the footwall and hanging wall blocks are offset like two seemingly rigid blocks. Coincidentally, faults rotate to shallower angles faster (per unit of horizontal extension) when the extension rate is lower. Finally, the regime boundary between long-lived faulting and multiple faults depends strongly on the extension rate multiplied by the faulted layer viscosity. In the following section, we use a simple scaling approach to gain insight into the extension rate-dependence of the viscoplastic simulations.

## 4 SEMI-ANALYTICAL SCALINGS TO GUIDE THE INTERPRETATION OF NUMERICAL SIMULATIONS

### 4.1 Fault-induced topography

In all our elastoplastic simulations topography grows in a rate-independent manner, suggesting that topography is driven entirely

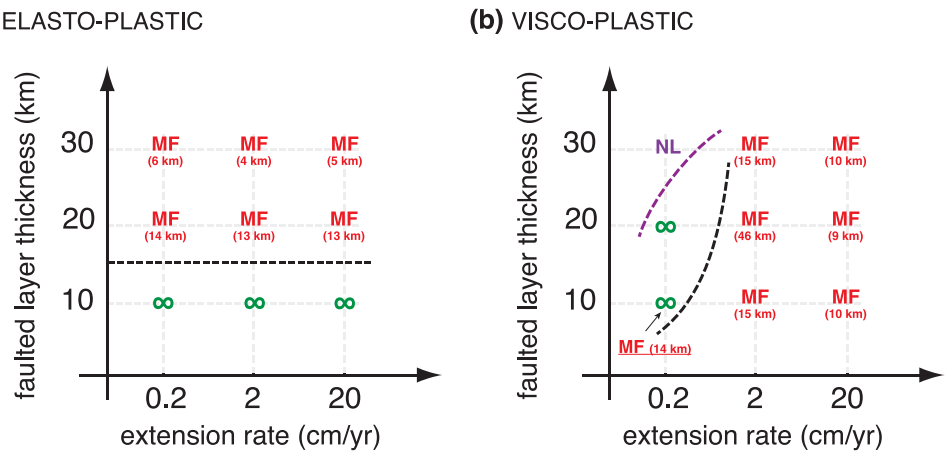


**Figure 6.** Regime diagrams for the life span of normal faults in (a) elastoplastic and (b) viscoplastic lithosphere, as a function of faulted layer thickness $H$ and full extension rate $U$. The 'prolonged-slip' regime ($\infty$) describes cases in which the initially seeded fault grows indefinitely; the 'multiple faults' (MF) regime refers to cases where the initial fault is abandoned in favour of a new, spontaneously forming fault. The horizontal offset accommodated on the initial fault when the next fault breaks is indicated in parentheses. NL refers to 'non-localized', a case where a shear band never cuts through the entire brittle layer (Fig. 3g). The faulted layer viscosity is $\eta_L = 10^{24}$ Pa s for all cases except the underlined case shown in the lower left with $H = 10$ km and $U = 0.2$ (label is offset for clarity and arrow points to the correct position on the diagram) in which $\eta_L = 10^{25}$ Pa s. The dashed black curve indicates a possible regime boundary between the prolonged-slip and the MF regime. The purple curve marks a possible criterion for localizing strain on the seeded fault (see Section 4.3 for details).

by elastic flexure. The fault-induced, flexural topography $w_T(x)$ is well explained by the thin plate solution of Weissel & Karner (1989) and detailed by Olive & Behn (2014):

$$w^T(x) = \frac{1}{4}\alpha_E \tan\theta \left( f\left|\frac{x - h/2}{\alpha_E}\right| - f\left|\frac{x + h/2}{\alpha_E}\right| \right) \tag{20}$$

with $f$ defined as

$$f(x) = e^{-x}(\sin x - \cos x)\,. \tag{21}$$

The flexure predicted by the numerical models closely resembles that predicted by eq. (20) (Figs 4a–d). To enable a quantitative comparison between the two models, we estimated the value of $\alpha_E$ that allows eq. (20) to best fit the numerical results presented in Figs 4(a)–(c), using a grid search approach. The elastic model best fits the elastoplastic simulations with 10-km-thick faulted layers with $\alpha_E = 20$ km across a wide range of extension rates and fault heaves. This value is slightly lower than the value of 28 km, which would be expected from eq. (18), if the numerical model were purely elastic. The mismatch likely represents the effect of diffuse plastic yielding (Fig. 2e) lowering the effective elastic thickness of the faulted layer (Buck 1988).

Our numerical results indicate that in the viscoplastic simulations the length scale of topographic decay decreases with time and is therefore not always accommodated within the numerical domain at the beginning of the simulations. In cases where viscous topographic decay occurs over a distance too broad for the domain size, topography appears flat on both sides of the fault, and the footwall and hanging wall effectively behave as two rigid blocks. We interpret the flat topography as an artefact of (1) the free-slip side boundary conditions allowing free uplift/subsidence along the sides of the box and (2) the uniform (horizontal) velocities applied along the sides, which may introduce moments that tend to flatten out the faulted layer near the boundaries. However, a no-slip boundary condition is not preferable, because pinning the edges of the layer often results in spurious plastic yielding along the sides of the model domain. In short, when the wavelength of topographic decay is longer than the model domain the boundary conditions likely introduce sizeable artefacts.

To understand the observed kinematics of the topographic decay in the viscoplastic cases, we derive an analytical solution for fault growth in a thin viscous plate. This is effectively a re-derivation of the classic Weissel & Karner (1989) elastic thin plate model using a viscous (Newtonian) rheology (Biot 1961; Turcotte & Schubert 2002). The solution is detailed in the Appendix. The key result is that the topographic decay of a viscous plate is well described by an elastic flexure model (eq. 20) with an effective 'viscous flexural wavelength' $\alpha_V$ that decreases with increasing fault heave, $h$ (Fig. 7) and depends on extension rate:

$$\alpha_V(h) = \left(\frac{\eta_L U H^3}{\Delta\rho g h}\right)^{\frac{1}{4}}. \tag{22}$$

The analytical result of a decreasing $\alpha_V$ with increasing $h$ is in agreement with the observation of topographic decay occurring on progressively shorter length scales as extension proceeds (Figs 4e–h), and on longer length scales in thicker faulted layers. The fact that $\alpha_V$ is a direct function of $U \times \eta_L$ is also consistent with the interchangeable effects of $U$ and $\eta_L$ on topography noted at the end of Section 3.2. To further test this model, we fit the topography presented in Figs 4(e)–(h) with the functional form of eq. (20), and estimate the flexural wavelength (here corresponding to an equivalent viscous flexural wavelength) that enables the best fit. Viscoplastic simulations with a 10-km-thick faulted layer initially produced rigid block topography, regardless of the extension rate. This topography, which is nearly flat on either side of the fault, can only be fit by eq. (20) when using an infinite flexural wavelength (dashed lines and diamonds in Fig. 7). However, as extension proceeds, the faulted layer bends on a shorter and shorter wavelength. When the extension rate is slow ($U = 0.2$ cm yr$^{-1}$), it only takes ~1 km of horizontal offset on the fault for the topographic decay to become resolvable within the numerical domain. With a faster extension rate (20 cm yr$^{-1}$), it takes about twice as much offset to resolve the topographic decay. The general trends of the numerical model results are captured by the analytical model represented by eq. (22), which shows a faster decay of the viscous flexural wavelength for smaller values of $U \times \eta_L$ (solid lines in Fig. 7). The analytical and

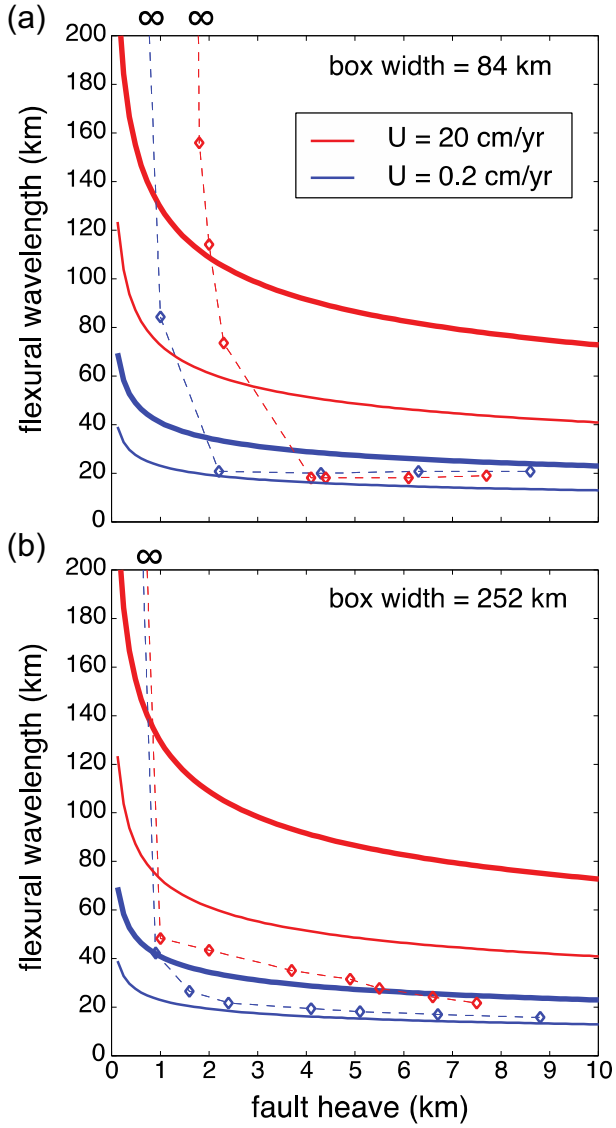


**Figure 7.** Flexural wavelength determined from fitting the topography produced in viscoplastic simulations ($\eta_L = 10^{24}$ Pa s, diamonds and dashed lines) with an analytical solution (eq. 20) at various amounts of fault heave for a numerical domain of width (a) 84 km, and (b) 252 km. Colored lines show the analytical prediction of eq. (22), using $\eta_L = 10^{24}$ Pa s (thick lines) and $10^{23}$ Pa s (thin lines). The colour code corresponds to varying extension rates. The faulted layer thickness is $H = 10$ km.

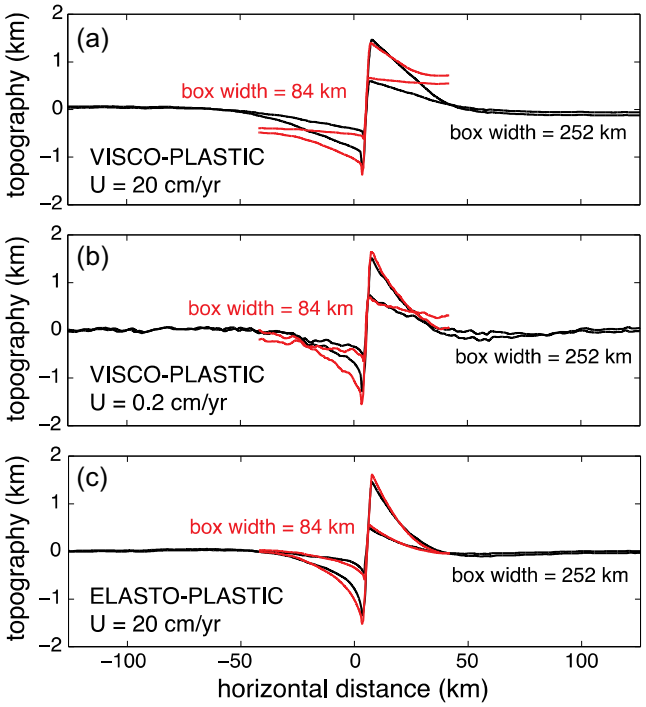


**Figure 8.** Model topography obtained after ~1 and ~2 km of extension on a fault cutting through a 10-km-thick faulted layer in a numerical domain that is either 84 (red) or 252 (black) km-wide. (a) and (b): Viscoplastic layers subjected to 20 and 0.2 cm yr$^{-1}$ of extension, respectively. (c) Elastoplastic layer subjected to 20 cm yr$^{-1}$ of extension.

numerical models, however, are in poor quantitative agreement. This is not surprising given the fact that the analytical model considers a thin, infinitely long plate of perfectly uniform viscosity, whereas the numerical model predicts diffuse plastic yielding, which decreases the effective viscosity in sizeable portions of the footwall and hanging wall blocks, as seen in Fig. 2(f).

An important corollary to these results is that the width of the numerical domain may strongly influence the behaviour of viscoplastic simulations of rifting. As a demonstration, we re-ran two viscoplastic simulations (and one elastoplastic simulation, for reference) in a domain three times wider than the original width of 84 km (runs ending in 'LB' in Table 2). The corresponding fault-induced topographies are shown in Fig. 8. All these large box runs produced a well-expressed decay of topography away from the fault scarp. The topography produced in the elastoplastic run is unchanged by an increase in box size (Fig. 8c). This confirms that a box width of $L = 3\alpha_E$ is sufficient to accommodate elastoplastic bending within the numerical domain. On the other hand, the differences between the small and large boxes can be striking for viscoplastic runs. When the extension rate is high, the viscoplastic lithosphere in the small numerical domain initially behaves as rigid blocks (red profile in Fig. 8a). However, this effect is suppressed if the box width is increased (black profile in Fig. 8a).

Box width is less important if the extension rate is lower (Fig. 8b). As described earlier, we estimate the evolving flexural wavelength of these large box viscoplastic runs by fitting eq. (20) to the modelled topography at various stages of fault evolution. The results are plotted in Fig. 7(b). Again, we observe a faster decay of the flexural wavelength with increasing fault heave when the extension rate is lower. This decay is faster in the large box runs (Fig. 7b) than in their small box counterparts (Fig. 7a). In the large box runs, the measured viscous flexural wavelengths (20–60 km) are more consistent with the analytical predictions over a wider range of heaves ($h > 2$ km), provided one assumes a faulted layer viscosity of $10^{23}$ Pa s in the analytical model instead of the value of $10^{24}$ Pa s used in the numerical simulations. This discrepancy is likely due to the effect of diffuse plastic yielding lowering the effective viscosity of the faulted layer (Fig. 2f), just as it decreases the effective elastic thickness in the elastoplastic simulations.

These simulations with varying box sizes demonstrate that using a domain width that can accommodate at least ~3 flexural wavelengths is essential to obtain realistic topographies in models of tectonic extension. In viscoplastic layers, using a greater box width enables the model to accommodate the full topographic decay earlier starting at a smaller amount of heave, and to restrict the initial rigid blocks phase to a minimum duration.

### 4.2 Fault rotation

In all elastoplastic simulations, the initial fault (dipping ∼50°) rotates rapidly towards a shallower dip ≤40° (Fig. 5a). We interpret this behaviour to result from the passive advection of the fault plane in the displacement field induced by footwall and hanging wall flexure, which simultaneously acts to minimize the total work done by the system (Olive & Behn 2014). Olive *et al*. (2014) demonstrated that with this mechanism, the fault rotation rate $\partial\theta/\partial h$ scales as the inverse of the flexural wavelength of the faulted layer. This mechanism accounts for the faster rotation rates measured in both the viscoplastic simulations conducted at slower extension rates (Figs 5b and c) and in thinner brittle layers (Fig. 5d), because decreasing $U$, $H$ or both parameters results in a decrease in the viscous flexural wavelength (eq. 22).

In order to gain a more quantitative understanding of rotation kinematics in a viscous faulted layer, we incorporate the heave-dependent flexural wavelength derived in the Appendix into the kinematic fault rotation model of Olive *et al*. (2014). We expect the temporal rate of fault rotation to roughly scale with the average rotation rate of the near-fault displacement field, $\dot{\Omega}$:

$$\frac{\partial\theta}{\partial t} \sim -\dot{\Omega}. \tag{23}$$

To first order, the main source of rotation is the lateral gradient of vertical motion, which is maximal at the fault (equal to $0.5U\tan\theta$), and becomes negligible a fraction ($\Phi$) of the flexural wavelength $\alpha$ away from the fault. The length scale $\Phi\alpha$ can thus be thought of as the lever arm involved in the rotation of the fault. We therefore write

$$\dot{\Omega} \approx \frac{1}{2}\frac{\partial v_y}{\partial x} \approx \frac{1}{4}\frac{U\tan\theta}{\Phi\alpha}. \tag{24}$$

Substituting eq. (24) into eq. (23) with the constraint $h = Ut$ yields

$$\frac{\partial\theta}{\partial h} = -\frac{\tan\theta}{4\Phi\alpha}, \tag{25}$$

which can be integrated to yield

$$\theta = \sin^{-1}\left[\sin\theta_0 \exp\left(-\frac{1}{4\Phi}\int_0^h \frac{\mathrm{d}h}{\alpha(h)}\right)\right]. \tag{26}$$

With these assumptions, we can predict the evolution of fault dip as a function of heave for a given extension rate. In a purely elastic lithosphere, the flexural wavelength is a constant given by eq. (18), and eq. (26) simplifies to

$$\theta = \sin^{-1}\left[\sin\theta_0 \exp\left(-\frac{h}{4\Phi\alpha_E}\right)\right]. \tag{27}$$

By contrast, for a purely viscous lithosphere, we substitute eq. (22) into eq. (26) to yield

$$\theta = \sin^{-1}\left[\sin\theta_0 \exp\left(-\frac{1}{5\Phi}\left(\frac{\Delta\rho g}{\eta_L U H^3}\right)^{\frac{1}{4}} h^{\frac{5}{4}}\right)\right]. \tag{28}$$

Following the approach of Olive *et al*. (2014), we assume a scaling factor $\Phi = 0.25$, which was empirically found to accurately predict fault rotation rates in elastoplastic simulations across a range of faulted layer thicknesses. A value of 0.25 means that the lever arm associated with fault rotation corresponds to about a fourth of the effective flexural wavelength of the faulted layer (eq. 22).

Fig. 5 shows the comparison between our analytical prediction of fault rotation and numerical results. The extension rate-independent rotation observed in elastoplastic numerical simulations is well explained by our simple elastic model (Fig. 5a); it also indicates that the diffuse plasticity outside of the fault zone does not significantly influence fault rotation. The analytical model for fault rotation in viscous layers captures the slower rotation with accumulated fault heave in thicker layers (Fig. 5d).

Because the analytical rotation model suffers from the same limitations as the analytical topographic model (no plasticity, constant Newtonian viscosity, thin-plate approximation), the quantitative agreement between the analytical rotation kinematics and the numerical results is poor. Similar to the topography model (Fig. 7), the agreement between numerical simulations and analytical predictions is improved if a viscosity lower than $10^{24}$ Pa s is used in the analytical model (thin lines in Fig. 5). This is likely the signature of diffuse plastic yielding in the numerical models not included in the analytical models (Fig. 2f).

Finally, the difference in fault rotation rate resulting from a change in extension rate is better pronounced in the simulations carried out with a wider numerical domain (Fig. 5c). This suggests that the finite width of the numerical domain is another major contributor to the discrepancy between our analytical predictions and numerical results.

### 4.3 Fault life span

The control of layer thickness $H$ on fault life span in elastoplastic layers is well explained by the accumulation of elastic (rate-independent) stresses associated with lithospheric flexure and topographic growth (Forsyth 1992; Buck 1993; Lavier *et al*. 2000; Olive & Behn 2014; Olive *et al*. 2014). Specifically, Forsyth (1992) and Buck (1993) showed that sustaining topographic growth and bending the footwall and hanging wall blocks requires an increasing amount of force as the fault accumulates more offset. Lavier *et al*. (2000) established that the maximum force increase $\Delta F$ required to bend an elastoplastic layer scales with layer thickness according to:

$$\Delta F = \Pi H^2, \tag{29}$$

where $\Pi$ is a constant dependent on the elastoplastic properties of the layer (e.g. $\Pi$ increases with increasing shear or Young's modulus). They also estimated that the increase in force required to break a new fault in intact lithosphere $\Delta F_{\mathrm{BREAK}}$ should roughly scale with the strength contrast $\Delta\sigma_y$ between a weak fault zone and intact lithosphere integrated over the thickness of the faulted layer:

$$\Delta F_{\mathrm{BREAK}} = \Delta\sigma_y H. \tag{30}$$

If the maximum force increase due to bending during fault growth never exceeds $\Delta F_{\mathrm{BREAK}}$, a fault can grow indefinitely without being abandoned. The criterion for the prolonged slip regime is therefore

$$\Delta F < \Delta F_{\mathrm{BREAK}}. \tag{31}$$

In an elastoplastic layer, this translates as a criterion on layer thickness that does not depend on extension rate

$$H < \frac{\Delta\sigma_y}{\Pi}, \tag{32}$$

thereby explaining why prolonged slip only occurs in layers thinner than a critical value of $H$ between 10 and 20 km in our numerical simulations (Fig. 6a).

In a viscous layer, however, dimensional analysis shows that the maximum force increase associated with footwall and hanging wall deformation (i.e. the depth-integrated deviatoric stress) scales with the faulted layer viscosity times strain rate. The average strain rate in areas adjacent to the fault should scale with the extension rate

normalized by the domain width, resulting in the following scaling for $\Delta F$:

$$\Delta F \approx \frac{\eta_L U H}{L}. \quad (33)$$

In this case, the criterion for prolonged slip on the initial fault (eq. 31) translates into a critical extension rate rather than a critical layer thickness:

$$U < \frac{\Delta\sigma_y L}{\eta_L}. \quad (34)$$

This simple scaling is consistent with the regime boundary illustrated in Fig. 6(b). In our simulations, the critical extension rate is between 0.2 and 2 cm yr$^{-1}$ for $\eta_L = 10^{24}$ Pa s across a range of $L = 84$–$190$ km (Table 2). Since we set the domain width to three times the equivalent elastic flexural wavelength of the faulted layer, $L$ increases with layer thickness as $L \sim H^{\frac{3}{4}}$ (eq. 18). We therefore expect the critical extension (eq. 34) rate to increase with increasing $H$ in a concave up manner. This prediction is consistent with the fact that in run V20ref ($H = 20$ km, $U = 2$ cm yr$^{-1}$) the second fault formed after the initial fault accumulated a horizontal offset of ∼46 km, which is much greater than in any other fault observed in a 'multiple fault' regime simulation (Fig. 6b). For a layer thickness of 20 km, the transition between the two faulting regimes must therefore be very close to $U = 2$ cm yr$^{-1}$. Further, if $\eta_L$ is increased to $10^{25}$ Pa s, the critical rate drops below 0.2 cm yr$^{-1}$ (run V10slow_25 in Table 2), which is consistent with eq. (34).

Finally, this simple scaling approach may explain why viscoplastic simulation V30slow with a large box ($L = 190$ km) and the slowest extension rate ($U = 0.2$ cm yr$^{-1}$) did not result in full strain localization onto the fault seed in the first place (Fig. 3g); the imposed strain rate was so low that the stresses never fully exceeded the plastic failure point of the lithosphere. In order to drive strain localization on the entire fault seed, the force applied when imposing extension on the edges of the domain must exceed the integrated resistance of the layer, which scales as $\sim\mu\rho g H^2$. From eq. (33), we expect that the slowest extension rate at which localization can occur ($U_{\mathrm{LOC}}$) should scale as

$$U_{\mathrm{LOC}} \sim \frac{\mu\rho g H L}{\eta_L}. \quad (35)$$

This critical extension rate for localization should therefore increase with increasing layer thickness as $H^{\frac{7}{4}}$, that is, as a concave-down function of $H$. This is illustrated as a purple dashed curve in Fig. 6(b).

## 5 CONCLUDING REMARKS

This study addresses the differences between numerical simulations of tectonic extension in an elastoplastic and a viscoplastic lithosphere. We focus on the long-term evolution of individual normal faults, which constitute the building blocks of extensional plate boundaries. We show that elasticity promotes rift geometries (topography and fault rotation) that depend only on the total amount of extension and not on the rate of extension. Specifically, fault life span, and therefore the style of extensional faulting (multiple short-offset faults versus long-lived detachments) are unaffected by extension rate in elastoplastic simulations, and instead are strongly controlled by lithospheric thickness.

A viscoplastic rheology can often reproduce the qualitative behaviour of elastoplastic simulations, by displaying a pronounced topographic decay away from the fault scarp, and predicting faults to rotate rapidly after they localize. This behaviour is favoured when the numerical domain is wide enough to accommodate ∼3 times the effective flexural wavelength of the viscous layer, which decreases over time as predicted by eq. (22). If the model domain is not wide enough, the topography will initially mimic that of rigid blocks offset by the fault with little internal deformation (e.g. Behn *et al*. 2002). Further, we find that the faulting regime (Fig. 6, Table 2) in viscoplastic layers is primarily controlled by the product of layer viscosity and extension rate, and is only weakly sensitive to faulted layer thickness.

The elastoplastic prediction of rate-independent fault evolution is most relevant to natural continental rift and mid-ocean ridge settings, given that the characteristic topographic signature of elastic flexure is observed near normal faults over a wide range of spreading rates (e.g. King *et al*. 1988; Weissel & Karner 1989; Armijo *et al*. 1996; Schouten *et al*. 2010). Further, the differences in rift morphology across spreading rates are generally well explained by rheological factors (i.e. lithospheric thickness) and external controls such as magmatism (Buck *et al*. 2005; Behn & Ito 2008; Ito & Behn 2008) and surface processes (Olive *et al*. 2014).

Some authors have proposed that extension rate itself may exert a rheological control on mid-ocean ridge morphology and the development of transform faults (Gerya 2010b, 2013; Püthe & Gerya 2013). However, this suggestion is based upon numerical models that do not include elasticity, and should therefore be examined in light of our new results and scalings. The moderately low lithospheric viscosity (∼$10^{22}$ Pa s) and relatively thin layer thickness (∼10 km) used by Püthe & Gerya (2013) guarantees that the viscous flexural wavelength of the lithosphere is rapidly accommodated within the model domain (∼100 km). These simulations can therefore produce topography that qualitatively resembles elastic flexure, yet the results of our study raise questions as to what extent the prediction of a spreading rate-dependent ridge morphology found by Püthe & Gerya (2013) results from the use of a viscoplastic approximation to the natural rheology of oceanic plates.

In a broad sense, the analogies between elastoplastic and viscoplastic models result from mathematical similarities between linear elasticity (stress proportional to strain) and Newtonian viscosity (stress proportional to strain rate). However, these similarities are at risk of breaking down in a problem-dependent manner when key parameters such as lithospheric thickness or velocity boundary conditions are changed. Further, the incorporation of elasticity in a numerical model can significantly affect the spatial and temporal evolution of deviatoric stresses, which in turn control the formation of new faults. Elasticity is therefore critically important in long-term geodynamic simulations that involve faults forming in a sequence and significantly deforming the surrounding lithosphere. Fortunately, viscoelastoplastic codes are becoming widely available to the long-term tectonics community—for example Cundall (1989, FLAC); Gerya & Yuen (2003, 2007; Gerya 2010a, I2ELVIS and I3ELVIS); Moresi *et al*. (2007, Underworld); Dabrowski *et al*. (2008), Kaus (2010, MILAMIN_VEP); Choi *et al*. (2008, SNAC; 2013, DynEarthSol2D); May *et al*. (2014, pTatin3D).

Lastly, we acknowledge that the cases investigated here are end members in which the lithosphere is entirely elastic–brittle, or viscous–brittle. Quantifying the behaviour of the more realistic, intermediate case of a viscoelastoplastic layer (in which the hotter, lower portion of the lithosphere fails by more or less distributed viscous creep) is beyond the scope of this study. A first step towards this goal would be to elucidate the fundamental mechanics of stress coupling across the brittle–ductile transition, which remain poorly understood (e.g. Nagel & Buck 2006).

## ACKNOWLEDGEMENTS

The authors wish to thank John D. Platt and Lucas Willemsen for helpful discussions regarding the analytical modelling. We also thank Boris Kaus and an anonymous reviewer for their valuable feedback. This work was supported by NSF grants OCE-11-54238 (JAO, MDB), EAR-10-10432 (MDB) and OCE-11-55098 (GI), as well as a WHOI Deep Exploration Institute grant and start-up support from the University of Idaho (EM). MATLAB is a registered trademark of The MathWorks, Inc.

## REFERENCES

Allken, V., Huismans, R.S. & Thieulot, C., 2011. Three-dimensional numerical modeling of upper crustal extensional systems, *J. geophys. Res.,* **116,** B10409, doi:10.1029/2011JB008319.

Allken, V., Huismans, R.S. & Thieulot, C., 2012. Factors controlling the mode of rift interaction in brittle-ductile coupled systems: a 3D numerical study, *Geochem. Geophys. Geosyst.,* **13**(5), Q05010, doi:10.1029/2012GC004077.

Allken, V., Huismans, R.S., Fossen, H. & Thieulot, C., 2013. 3D numerical modelling of graben interaction and linkage: a case study of the Canyonlands grabens, Utah, *Basin Res*., **25,** 1–14.

Armijo, R., Meyer, B., King, G.C.P., Rigo, A. & Papanastassiou, D., 1996. Quaternary evolution of the Corinth Rift and its implications for the late Cenozoic evolution of the Aegean, *Geophys. J. Int.,* **126**(1), 11–53.

Behn, M.D. & Ito, G., 2008. Magmatic and tectonic extension at mid-ocean ridges: 1. Controls on fault characteristics, *Geochem. Geophys. Geosyst.,* **9,** Q08O10, doi:10.1029/2008GC001965.

Behn, M.D., Lin, J. & Zuber, M.T., 2002. A continuum mechanics model for normal faulting using a strain-rate softening rheology: implications for thermal and rheological controls on continental and oceanic rifting, *Earth planet. Sci. Lett.,* **202,** 725–740.

Behn, M.D., Boettcher, M.S. & Hirth, G., 2007. On the thermal structure of oceanic transform faults, *Geology,* **35,** 307–310.

Billen, M., 2008. Modeling the dynamics of subducting slabs, *Annu. Rev. Earth Sci.,* **36,** 325–356.

Biot, M.A., 1961. Theory of folding of stratified viscoelastic media and its implications in tectonics and orogenesis, *Geol. Soc. Am. Bull.,* **72,** 1595–1620.

Buck, W.R., 1988. Flexural rotation of normal faults, *Tectonics,* **7**(5), 959–973.

Buck, W.R., 1993. Effect of lithospheric thickness on the formation of high- and low-angle normal faults, *Geology,* **21**(10), 933–936.

Buck, W.R., Lavier, L.L. & Poliakov, A.N.B., 2005. Modes of faulting at mid-ocean ridges, *Nature,* **434,** 719–723.

Choi, E., Lavier, L.L. & Gurnis, M., 2008. Thermomechanics of mid-ocean ridge segmentation, *Phys. Earth planet. Inter.,* **171,** 374–386.

Choi, E., Tan, E., Lavier, L.L. & Calo, V.M., 2013. DynEarthSol2D: an efficient unstructured finite element method to study long-term tectonic deformation, *J. geophys. Res.,* **118,** 1–16.

Crameri, F. *et al.*, 2012. A comparison of numerical surface topography calculations in geodynamic modelling: an evaluation of the 'sticky air' method, *Geophys. J. Int.,* **189,** 38–54.

Cundall, P.A., 1989. Numerical experiments on localization in frictional materials, *Ingenieur Archiv,* **59,** 148–159.

Dabrowski, M., Krotkiewski, M. & Schmid, D.W., 2008. MILAMIN: MATLAB-based FEM solver for large problems. *Geochem. Geophys. Geosyst.,* **9**(4), doi:10.1029/2007GC001719.

Duretz, T., May, D.A., Gerya, T.V. & Tackley, P.J., 2011. Discretization errors and free surface stabilization in the finite difference and marker-in-cell method for applied geodynamics: a numerical study, *Geochem. Geophys. Geosyst.,* **12**(7), Q07004, doi:10.1029/2011GC003567.

Farrington, R.J., Moresi, L.-N. & Capitanio, F.A., 2014. The role of viscoelasticity in subducting plates, *Geochem. Geophys. Geosyst.,* **15**(11), 4291–4304.

Forsyth, D.W., 1992. Finite extension and low-angle normal faulting, *Geology,* **20**(1), 27–30.

Fourel, L., Goes, S. & Morra, G., 2014. The role of elasticity in slab bending, *Geochem. Geophys. Geosyst.,* **15**(11), 4507–4525.

Gerya, T.V., 2010a. *Introduction to Numerical Geodynamic Modelling,* Cambridge Univ. Press.

Gerya, T.V., 2010b. Dynamical instability produces transform faults at mid-ocean ridges, *Science,* **329,** 1047–1050.

Gerya, T.V., 2013. Three-dimensional thermomechanical modeling of oceanic spreading initiation and evolution, *Phys. Earth planet. Inter.,* **214,** 35–52.

Gerya, T.V. & Yuen, D.A., 2003. Characteristics-based marker-in-cell method with conservative finite-differences schemes for modeling geological flows with strongly variable transport properties, *Phys. Earth planet. Inter.,* **140,** 293–318.

Gerya, T.V. & Yuen, D.A., 2007. Robust characteristics method for modelling multiphase visco-elasto-plastic thermo-mechanical problems, *Phys. Earth planet. Inter.,* **163,** 83–105.

Goetze, C. & Evans, E., 1979. Stress and temperature in the bending lithosphere as constrained by experimental rock mechanics, *Geophys. J. R. astr. Soc.,* **59**(3), 463–478.

Harlow, F.H. & Welch, J.E., 1965. Numerical calculation of time-dependent viscous incompressible flow of fluid with free surface, *Phys. Fluids,* **8**(12), 2182–2189.

Ito, G. & Behn, M.D., 2008. Magmatic and tectonic extension at mid-ocean ridges: 2. Origin of axial morphology, *Geochem. Geophys. Geosyst.,* **9,** Q08O10, doi:10.1029/2008GC001970.

Kaus, B.J.P., 2010. Factors that control the angle of shear bands in geodynamic numerical models of brittle deformation, *Tectonophysics,* **484,** 36–47.

Kaus, B.J.P. & Becker, T.W., 2007. Effects of elasticity on the Rayleigh-Taylor instability: implications for large-scale geodynamics, *Geophys. J. Int.,* **168,** 843–862.

Kaus, B.J.P. & Podlachikov, Y., 2006. Initiation of localized shear zones in viscoelastoplastic rocks, *J. geophys. Res.,* **111,** B04412, doi:10.1029/2005JB003652.

Keller, T., May, D.A. & Kaus, B.J.P., 2013. Numerical modelling of magma dynamics coupled to tectonic deformation of lithosphere and crust, *Geophys. J. Int.,* **195**(3), 1406–1442.

King, G.C.P., Stein, R.S. & Rundle, J.B., 1988. The growth of geological structures by repeated earthquakes 1. Conceptual framework, *J. geophys. Res.,* **93**(B11), 13 307–13 318.

King, G.C.P., Stein, R.S. & Lin, J., 1994. Static stress change and the triggering of earthquakes, *Bull. seism. Soc. Am.,* **84**(3), 935–953.

Lavier, L.L. & Buck, W.R., 2002. Half graben versus large-offset low-angle normal fault: importance of keeping cool during normal faulting, *J. geophys. Res.,* **107**(B6), doi:10.1029/2001JB000513.

Lavier, L.L., Buck, W.R. & Poliakov, A.N.B., 2000. Factors controlling normal fault offset in an ideal brittle layer, *J. geophys. Res.,* **105**(B10), 23 431–23 442.

May, D.A., Brown, J. & Le Pourhiet, L., 2014. pTatin3D: high-performance methods for long-term lithospheric dynamics, in *SC'14 Proceedings of the International Conference for High Performance Computing, Networking, Storage and Analysis,* New Orleans, pp. 274–284.

Moresi, L., Dufour, F. & Mühlhaus, H.-B., 2003. Lagrangian integration point finite element method for large deformation modeling of viscoelastic geomaterials, *J. Comp. Phys.,* **184,** 476–497.

Moresi, L., Quenette, S., Lemiale, V., Mériaux, C., Appelbe, W. & Mühlhaus, H.-B., 2007. Computational approaches to studying non-linear dynamics of the crust and mantle, *Phys. Earth planet. Inter.,* **163,** 69–82.

Murrell, S.A.F., 1976. Rheology of the lithosphere—experimental indications, *Tectonophysics,* **36,** 5–24.

Nagel, T.J. & Buck, W.R., 2006. Channel flow and the development of parallel normal faults, *J. geophys. Res.,* **111,** B08407, doi:10.1029/2005JB004000.

Olive, J.-A. & Behn, M.D., 2014. Rapid rotation of normal faults due to flexural stresses: an explanation for the global distribution of normal fault dips, *J. geophys. Res.,* **119,** doi:10.1002/2013JB010512.

Olive, J.-A., Behn, M.D. & Malatesta, L.C., 2014. Modes of extensional faulting controlled by surface processes, *Geophys. Res. Lett.,* **41**(19), 6725–6733.

Poliakov, A.N.B. & Buck, W.R., 1998. Mechanics of stretching elastic-plastic-viscous layers: applications to slow-spreading mid-ocean ridges, in *Faulting and Magmatism at Mid-Ocean Ridges, Geophys. Monogr. Ser.,* Vol. 106, pp. 305–323, eds, Buck, W.R. *et al.*, AGU.

Püthe, C. & Gerya, T.V., 2013. Dependence of mid-ocean ridge morphology on spreading rate in numerical 3-D models, *Gondwana Res.*, **25,** 270–283.

Ranero, C.R., Phipps Morgan, J., McIntosh, K. & Reichert, C., 2003. Bending-related faulting and mantle serpentinization at the Middle America trench, *Nature,* **425,** 367–373.

Schmalholz, S.M. & Podlachikov, Y., 1999. Buckling versus folding: importance of viscoelasticity, *Geophys. Res. Lett.,* **26**(17), 2641–2644.

Schouten, H., Smith, D.K., Cann, J.R. & Escartin, J., 2010. Tectonic versus magmatic extension in the presence of core complexes at slow-spreading ridges from a visualization of faulted seafloor topography, *Geology,* **38**(7), 615–618.

Segall, P., 2010. *Earthquake and Volcano Deformation,* Princeton Univ. Press.

Turcotte, D.L. & Schubert, G., 2002. *Geodynamics,* 2nd edn, Cambridge Univ. Press.

Watts, A.B., 2001. *Isostasy and Flexure of the Lithosphere,* Cambridge Univ. Press.

Watts, A.B. & Burov, E.B., 2003. Lithospheric strength and its relationship to the elastic and seismogenic layer thickness, *Earth planet. Sci. Lett.,* **213,** 113–131.

Watts, A.B. & Zhong, S., 2000. Observations of flexure and the rheology of oceanic lithosphere, *J. geophys. Res.,* **142,** 855–875.

Weissel, J.K. & Karner, J.D., 1989. Flexural uplift of rift flanks due to mechanical unloading of the lithosphere during extension, *J. geophys. Res.,* **94**(B10), 13 919–13 950.

Zhang, F., Lin, J. & Zhan, W., 2014. Variations in oceanic plate bending along the Mariana trench, *Earth planet. Sci. Lett.,* **401,** 206–214.

Zhou, Z., Lin, J., Behn, M.D. & Olive, J.-A., 2015. Mechanism for normal faulting in the subducting plate at the Mariana Trench, *Geophys. Res. Lett.,* **42,** doi:10.1002/2015GL063917.

## APPENDIX: FAULT-INDUCED TOPOGRAPHY IN A VISCOUS LITHOSPHERE

The plate deflection resulting from slip on a fault is modelled by adding the contribution of (a) rigid motion of the hanging wall and footwall blocks along the fault and (b) viscous deformation of the footwall and hanging wall blocks in response to gravity (Weissel & Karner 1989). If $w^*(x,t)$ denotes the topography resulting from step (a) alone, the deflection $w(x,t)$ corresponding to step (b) can be calculated as the response to the load exerted by $w^*(x,t)$. In a viscous faulted layer, $w(x,t)$ is the solution to the thin viscous plate equation (Biot 1961; Turcotte & Schubert 2002)

$$F\frac{\partial^4 \dot{w}}{\partial x^4} + \Delta\rho g w = -\Delta\rho g w^* \tag{A1}$$

where $F$ denotes the viscous equivalent to the elastic flexural rigidity $D$ (eq. 13)

$$F = \frac{1}{6}\eta_{\mathrm{L}} H^3 \tag{A2}$$

and $w^*(x,t)$ is

$$w^*(x,t) = \begin{cases} -\frac{Ut}{2}\tan\theta, & \forall x \le -\frac{Ut}{2} \\ x\tan\theta, & \forall x \in \left[-\frac{Ut}{2}, \frac{Ut}{2}\right] \\ \frac{Ut}{2}\tan\theta, & \forall x \ge \frac{Ut}{2} \end{cases} \tag{A3}$$

In this notation, $U$ denotes the full extension rate, $t$ is the time since the onset of faulting and $x$ originates where the fault initially intersects the surface (Table 1). The resulting, fault-induced topography $w^{\mathrm{T}}(x,t)$ is then obtained by adding increments of $w^*(x,t)$ and $w(x,t)$, following

$$\frac{\partial w^T}{\partial t} = \frac{\partial w}{\partial t} + \frac{\partial w*}{\partial t} \tag{A4}$$

In the following, we outline a semi-analytical method to solve (A1)–(A4) using Laplace and Fourier transforms. The problem is reduced to the calculation of an inverse Fourier transform, which can be estimated numerically. We then propose an approximate solution that captures the behaviour of the exact solution and is easier to implement in simple scaling models.

For any function $f(x,t)$ we write $\hat{f}(k,t)$ its Fourier transform defined as

$$\hat{f}(k,t) = \frac{1}{\sqrt{2\pi}}\int_{-\infty}^{+\infty} f(x,t)\mathrm{e}^{\mathrm{i}kx}\mathrm{d}x \tag{A5}$$

and the inverse Fourier transform is defined by

$$f(x,t) = \frac{1}{\sqrt{2\pi}}\int_{-\infty}^{+\infty} \hat{f}(k,t)\mathrm{e}^{-\mathrm{i}kx}\mathrm{d}k. \tag{A6}$$

The Laplace transform $\tilde{f}(x,s)$ is defined as

$$\tilde{f}(x,s) = \int_0^{+\infty} f(x,t)\mathrm{e}^{-st}\mathrm{d}t. \tag{A7}$$

Taking the Laplace and Fourier transforms, successively, of eq. (A1) yields

$$\hat{\tilde{w}} = \frac{-\Delta\rho g}{k^4 F s + \Delta\rho g}\hat{\tilde{w}}^*. \tag{A8}$$

In order to calculate the Laplace transform of $w^*(x,t)$ (eq. A3), we rewrite it as an explicit function of time:

$$w^*(x,t) = \begin{cases} \mathrm{sgn}(x)\frac{Ut}{2}\tan\theta, & \forall t \le \left|\frac{Ux}{2}\right| \\ x\tan\theta, & \forall t \ge \left|\frac{2x}{U}\right| \end{cases}. \tag{A9}$$

Piece-wise integration yields

$$\tilde{w}^*(x,s) = \frac{U}{2s^2}\tan\theta\left(1 - \mathrm{e}^{-\left|\frac{2xs}{U}\right|}\right) \times \mathrm{sgn}\left(\frac{2xs}{U}\right). \tag{A10}$$

Finally, the Fourier transform of eq. (A10) is found to be

$$\hat{\tilde{w}}^*(k,s) = \frac{Ui\tan\theta}{k\sqrt{2\pi}} \times \frac{1}{\left(s + i\frac{Uk}{2}\right)\left(s - i\frac{Uk}{2}\right)}. \tag{A11}$$

Using eq. (A8), we can now write $\hat{\tilde{w}}^*(k,s)$

$$\hat{\tilde{w}}(k,s) = \frac{iU\Delta\rho g\tan\theta}{k^5 F\sqrt{2\pi}} \times \frac{1}{\left(s + \frac{\Delta\rho g}{k^4 F}\right)\left(s + i\frac{Uk}{2}\right)\left(s - i\frac{Uk}{2}\right)}. \tag{A12}$$

We note that the $s$-dependence of eq. (A12) is a rational fraction that we can expand into a sum of partial fractions. We can then identify a sum of tabulated Laplace transforms, which are readily inverted into time domain. By applying the inverse Fourier transform formula (eq. A6), we can reduce the calculation of $w(x,t)$ to the estimation of an integral, which can be performed numerically:

$$w(x,t) = -\frac{iU\Delta\rho g\tan\theta}{2\pi F} \times \int_{-\infty}^{+\infty} \frac{1}{k^5}\left(\frac{1}{iUk\left(A(k) + \frac{iUk}{2}\right)}\mathrm{e}^{\frac{iUkt}{2}}\right.$$
$$\left. - \frac{1}{iUk\left(A(k) - \frac{iUk}{2}\right)}\mathrm{e}^{-\frac{iUkt}{2}} + B(k)\right)\mathrm{e}^{-\mathrm{i}kx}\mathrm{d}k \tag{A13}$$

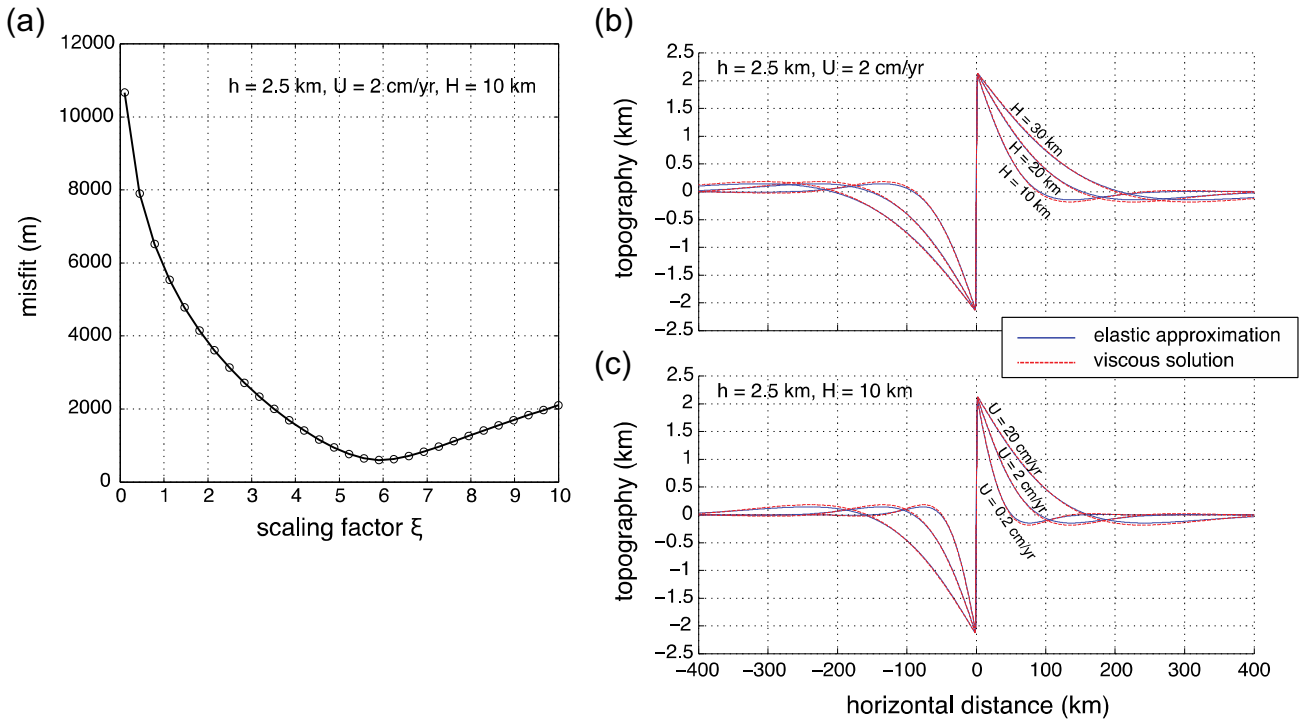


**Figure A1.** (a) Illustrative rms misfit between the exact solution to the viscous faulting problem [calculated from eq. (A13) through numerical integration] and the approximate solution (eq. A20 using the viscous flexural wavelength $\alpha_V$ from eq. A19 instead of $\alpha_E$) using various scaling factors $\xi$. This example corresponds to a fault heave of 2.5 km in a 10-km-thick layer with a viscosity of $10^{24}$ Pa s extended at a full rate of 2 cm yr$^{-1}$. (b) and (c): Topographies predicted by the exact solution (red) and the approximate solution using $\xi = 6$ (blue) for a range of layer thicknesses $H$ and extension rates $U$.

with

$$A(k) = \frac{\Delta\rho g}{k^4 F} \tag{A14}$$

and

$$B(k) = \frac{1}{\left(A(k) + \frac{iUk}{2}\right)\left(A(k) - \frac{iUk}{2}\right)} e^{-A(k)t}. \tag{A15}$$

Eq. (A13), however, does not allow straightforward comparisons between the topographies that develop in a viscous versus an elastic faulted layer. To enable such comparisons, we seek to extract a characteristic length scale for topographic decay in viscous plates that is analogous to the flexural wavelength of elastic plates. To do so, we note that the use of the Laplace transform makes the present derivation very similar to the case of an elastic thin plate, which would be characterized by the following flexure equation:

$$D\frac{\partial^4 w}{\partial x^4} + \Delta\rho g w = -\Delta\rho g w^* \tag{A16}$$

which can be expressed in Fourier domain:

$$\hat{w} = \frac{-\Delta\rho g}{k^4 D + \Delta\rho g}\hat{w}^*. \tag{A17}$$

Eq. (A17) has the same form as eq. (A8) provided $D$ is replaced by $Fs$. This suggests that the elastic solution with a time-dependent flexural rigidity is a good approximation for the viscous problem. From dimensional analysis, we propose an equivalent viscous rigidity of the form

$$D_V(t) = \frac{F}{t} = \frac{\eta_L H^3}{6t}. \tag{A18}$$

By analogy, we define a time-dependent viscous bending wavelength as

$$\alpha_V = \left(\frac{\zeta F}{\Delta\rho g t}\right)^{\frac{1}{4}}, \tag{A19}$$

where $\zeta$ is a scaling factor. We next recall the elastic solution to eq. (A17) outlined in Olive & Behn (2014):

$$w^T(x) = \frac{1}{4}\alpha_E \tan\theta \left(f\left|\frac{x - h/2}{\alpha_E}\right| - f\left|\frac{x + h/2}{\alpha_E}\right|\right) \tag{A20}$$

with $f$ defined as

$$f(x) = e^{-x}(\sin x - \cos x). \tag{A21}$$

We compare our exact solution (eq. A13) to the elastic solution using the time-dependent wavelength $\alpha_V$ defined in eq. (A19) instead of the elastic wavelength $\alpha_E$. We find that eq. (A20) provides the best approximation for the exact solution when $\alpha_V$ is calculated with a scaling factor $\zeta \approx 6$ (Fig. A1). We therefore propose the following definition for the viscous bending wavelength, which is used throughout the main text:

$$\alpha_V = \left(\frac{\eta_L H^3}{\Delta\rho g t}\right)^{\frac{1}{4}}. \tag{A22}$$

Finally, because fault heave ($h$) is more useful than time to describe experiments carried out at different extension rates, we rewrite (A22) as

$$\alpha_V = \left(\frac{\eta_L U H^3}{\Delta\rho g h}\right)^{\frac{1}{4}}. \tag{A23}$$